

# EGOC inhibits TOROID polymerization by structurally activating TORC1

**Manoël Prouteau**

University of Geneva

**Clélia Bourgoint**

University of Geneva

**Jan Felix**

VIB-UGent Center for Inflammation Research <https://orcid.org/0000-0002-8436-9467>

**Lenny Bonadei**

University of Geneva

**Yashar Sadian**

University of Geneva

**Caroline Gabus**

ENS-Lyon

**Savvas Savvides**

Ghent University <https://orcid.org/0000-0003-3420-5947>

**Irina Gutsche**

Institut de Biologie Structurale <https://orcid.org/0000-0002-1908-3921>

**Ambroise Desfosses**

Institut de Biologie Structurale <https://orcid.org/0000-0002-6525-5042>

**Robbie Loewith** (✉ [Robbie.Loewith@unige.ch](mailto:Robbie.Loewith@unige.ch))

University of Geneva <https://orcid.org/0000-0002-2482-603X>

---

## Article

### Keywords:

**Posted Date:** February 2nd, 2022

**DOI:** <https://doi.org/10.21203/rs.3.rs-1238390/v1>

**License:**   This work is licensed under a Creative Commons Attribution 4.0 International License.

[Read Full License](#)

---

**Version of Record:** A version of this preprint was published at Nature Structural & Molecular Biology on January 26th, 2023. See the published version at <https://doi.org/10.1038/s41594-022-00912-6>.

# Abstract

Target Of Rapamycin Complex 1 (TORC1) is a protein kinase controlling cell homeostasis and growth in response to nutrients and stresses. Glucose depletion triggers a pronounced redistribution of TORC1 from a dispersed localisation over the vacuole surface into a large, inactive condensate called a TOROID (TORC1 Organised in Inhibited Domain). However, the molecular mechanisms governing this transition were unclear. Here, we show that acute depletion and repletion of EGO Complex (EGOC) activity is sufficient to control TOROID distribution, independently of other nutrient-signalling pathways. A 3.8 Å-resolution 3D reconstruction of TORC1 from TOROID cryo-EM data together with interrogation of key interactions in vivo provided structural insights into TORC1-TORC1' and TORC1-EGOC interaction interfaces. These data support a model in which glucose-dependent activation of EGOC triggers binding to TORC1 at an interface required for TOROID assembly, resulting in inhibition of TORC1 polymerisation and release of active TORC1 dimers.

## Introduction

The Target Of Rapamycin, TOR, is a Phosphatidylinositol Kinase related protein Kinase (PIKK) family member<sup>1,2</sup> as it resembles lipid kinases but is rather a Ser/Thr protein kinase. Similarly to other PIKKs, TOR functions as the catalytic subunit of distinct multiprotein complexes, TORC1 and TORC2. These complexes are broadly conserved across eukaryote evolution, however, the rapamycin-sensitivity of TORC1 has facilitated studies of this complex and consequently TORC1 signalling is relatively better characterized compared to rapamycin-insensitive TORC2<sup>3,4</sup>. Both complexes are essential regulators of cell homeostasis: in yeast, TORC1 controls cell mass and volume according to nutrient availabilities and abiotic stresses while TORC2 maintains biophysical properties of the plasma membrane<sup>5</sup>.

Yeast TORC1 is composed of four proteins: either of the two TOR paralogs Tor1 or Tor2, Kog1, Lst8, and Tco89<sup>6,7</sup>. In humans, mTORC1 (mammalian/mechanistic Target Of Rapamycin Complex 1) respectively contains mTOR, Raptor and mLst8; a Tco89 orthologue is not apparent. TORC1 phosphorylates the AGC-family kinase Sch9 which served as a convenient reporter to demonstrate that TORC1 is active in the presence of good carbon (glucose), nitrogen (glutamine), and phosphate sources and inactivated upon nutrient deprivation as well as exposure to osmotic, redox or thermal stresses<sup>8</sup>. Sch9 and other TORC1 effectors subsequently regulate a plethora of molecular processes ranging from ribosome biogenesis to autophagy; from lipid biosynthesis to membrane trafficking<sup>9-12</sup>. mTORC1, which also phosphorylates an AGC-family kinase, S6K1, is additionally regulated downstream of growth-factor signalling and loss of mTORC1 regulation has been implicated in a large range of illnesses including cancers, neurodegenerative diseases and metabolic disorders<sup>13</sup>. Given its central role in physiological and pathophysiological growth control, molecular dissection of (m)TORC1 signalling is of considerable interest.

Structures of mTORC1 have been recently solved by combinations of X-ray crystallography and electron cryo-microscopy (cryo-EM) <sup>14-16</sup>. These studies demonstrated that mTORC1 is dimeric and, when bound, the macrolide rapamycin recruits the 12 kDa proline isomerase FKBP12 such that substrate access to the kinase active site is sterically occluded. Under physiological conditions, mTORC1 activity is regulated through the actions of multiple GTPases. The Rheb GTPase couples growth factor and energy cues to mTORC1 with the binding of GTP-loaded Rheb leading to allosteric rearrangements that increase the kinase activity of mTORC1 <sup>16</sup>. In contrast, the RAG GTPases have a more nuanced role in mTORC1 regulation, primarily downstream of nutrient cues.

There are two sets of *RAG* paralogues in mammalian cells: *RAGA* and *RAGB*, and *RAGC* and *RAGD*. These proteins form obligate heterodimers with GTP-loading status determining the distance and relative orientation between the two G-domains <sup>17,18</sup>. Unlike other GTPases, the RAGs are not modified with lipid but are instead anchored to the lysosome membrane via the heteropentameric Ragulator complex <sup>19-21</sup>. Recent structures of the Raptor•RAG•Ragulator complex suggest that active RagA<sup>GTP</sup>/RagC<sup>GDP</sup> is able to bind the Armadillo (ARM) domain of Raptor and grasp onto a specific short  $\alpha$ -helical fragment termed the 'Claw' <sup>22,23</sup>. This binding recruits mTORC1 from a mysterious localization in the cytoplasm to the lysosome where it can be subsequently activated by Rheb<sup>GTP</sup>.

The regulation of TORC1 in *Saccharomyces cerevisiae* (budding yeast) does not completely parallel the situation in mammalian cells. In contrast to mammalian cells and *Schizosaccharomyces pombe* <sup>24</sup>, there are no reported roles for the budding yeast Rheb orthologue, Rhb1, in TORC1 regulation. Furthermore, yeast TORC1 appears to be constitutively localized to vacuole and/or endosome membranes, regardless of its activity status <sup>25,26</sup>. We recently reported that acute glucose starvation triggers the condensation of TORC1 into a large, vacuole-associated helical polymer we named a TOROID (TORC1 organised in Inhibited Domains; <sup>27</sup>. TOROID formation tracked with, and was necessary for, Sch9 dephosphorylation, implying that this polymerization was mechanistically responsible for TORC1 inactivation. Consistently, a low-resolution TOROID structure suggested that stacking of TORC1 protomers (i.e. dimers) into the TOROID polymer would sterically occlude access to the kinase active site analogously to rapamycin-FKBP12 binding <sup>27</sup>. TOROID formation was found to be dependent upon the two yeast RAG orthologues *GTR1* (*RAGA/B*) and *GTR2* (*RAGC/D*):  $\Delta gtr1 \Delta gtr2$  cells present constitutive TOROIDs even in the presence of glucose and are impaired in their ability to downregulate Sch9 phosphorylation upon glucose starvation <sup>27</sup>.

Gtr1 and Gtr2, like the RAGs, are obligate heterodimers anchored to the vacuolar membrane via the EGO ternary complex (EGO-TC, the functional equivalent of Ragulator) composed of Ego1, Ego2 and Ego3 <sup>28</sup>. Ego1 is myristoylated and palmitoylated on its N-terminal extremity, which serves to tether the complex to the vacuolar membrane <sup>29</sup>. The remainder of Ego1, together with Ego2 and Ego3, cradle the C-terminal dimerization domains of Gtr1 and Gtr2 <sup>28</sup>. This orientation exposes the N-terminal G-domains of Gtr1 and Gtr2 to upstream regulators as well as their effector, TORC1. The GTPase activating Proteins (GAPs) that act on Gtr1 (RagA/B) and Gtr2 (RagC/D) are SEACIT (GATOR1) and Lst4/7 (FNIP-FLCN) respectively

<sup>30,31</sup>. In contrast to the relatively well-understood and accepted GAPs, numerous Guanine nucleotide Exchange Factors (GEFs) that act on Gtr1 (RagA/B) have been reported <sup>18,25,31</sup>. A GEF for Gtr2 (RagC/D) may not be necessary as this GTPase appears to possess an intrinsically high dissociation constant for GDP <sup>32</sup>. Similar, but not identical to the situation in mammalian cells, guanine nucleotide loading status of the Gtrs appears to have a direct role on TORC1 localization in yeast. Indeed, expressing mutants that lock the Gtrs in an inactive, Gtr1<sup>GDP</sup>/Gtr2<sup>GTP</sup> conformation, TORC1 is concentrated in a TOROID punctum on the vacuolar membrane whereas in cells expressing active, Gtr1<sup>GTP</sup>/Gtr2<sup>GDP</sup>, TORC1 is diffusely localized over the surface of the vacuole <sup>27</sup>. Molecular details explaining how the EGO-TC / Gtrs (collectively known as the EGO Complex, EGOC) govern TOROID assembly, alone or in conjunction with other nutrient-regulated signalling pathways, remain unknown.

To specifically assess the contribution of the EGOC to TORC1 localization dynamics, independently of the multitude of other glucose-responsive signalling pathways <sup>33</sup>, we developed orthogonal approaches by which we could acutely abrogate or reintroduce EGOC activity. We observed that proteolytic shaving of the EGOC off of the vacuole membrane triggered TORC1 puncta (TOROID) formation while reintroduction of the EGOC to the vacuole membrane triggered puncta disassembly. We additionally observed that the EGOC co-localizes with TORC1 puncta in a Gtr-dependent fashion. To better characterize this interaction, we used cryo-EM to obtain a 3.8 Å-resolution structure of TORC1 from TOROID cryo-EM maps. We found that a central hub of interactions locks the Kog1 Armadillo (ARM) domain on top of the kinase domain of Tor2' and sterically occludes the kinase active site. CrispR/Cas9 mutagenesis and pull-down assays were used to verify these core features and additionally revealed that this same hub is engaged by the EGOC to mediate glucose-dependent regulation of TORC1 signalling. Based on these data, we propose that the EGOC is necessary and sufficient for TOROID regulation through competition for a common binding hub in Kog1; trans binding of this hub to Tor1'/2' sequesters TORC1 into an inactive TOROID, while binding to active EGOC liberates TORC1 dimers able to signal to downstream targets.

## Results

### **Acute abrogation or restoration of EGOC activity on the vacuole membrane impacts TOROID dynamics independently of glucose changes**

We previously proposed that TOROID regulation downstream of glucose-derived signals was mediated via the EGOC <sup>27</sup>. This was based on constitutive presence of TOROIDs in  $\Delta gtr1 \Delta gtr2$  cells and an inability of cells expressing GTP/GDP-locked Gtr1/2 mutants to regulate TOROID assembly/disassembly according to glucose cues. However, knowing that glucose signals regulate TORC1 activity via additional, parallel pathways including Snf1/AMPK and pH <sup>34,35</sup>, we wished to determine if orthogonal, glucose-independent manipulation of EGOC function alone would be sufficient to alter TOROID formation.

To rapidly abrogate EGOC signalling, we introduced a Tobacco Etch Virus (TEV) Protease cleavage site into the amino-terminal region of Ego1, downstream of the lipidation sites (Ego1<sup>TEV</sup>; Figure 1A and S1A)

<sup>28,36</sup>. TEV protease was expressed downstream of the *CTH2* promoter, whose tight repression by Fe<sup>2+</sup> is quickly reversed by addition of the iron chelator Bathophenanthrolinedisulfonic acid (BPS; <sup>37</sup>. Neither acute BPS treatment nor TEV protease induction affected TORC1 activity in otherwise *WT* cells (Figure S1B).

While the *EGO1*<sup>TEV</sup> allele *per se* does not display a phenotype, expression of the TEV protease renders these, but not *WT* cells, hypersensitive to rapamycin demonstrating a loss of EGO function similar to cells lacking functional EGO (Figure S1C; <sup>25,38</sup>. In *EGO1*<sup>TEV</sup> cells, prior to TEV induction, the EGO was diffusely localized around the vacuole membrane; this signal was diminished by 50% after 30 minutes of TEV induction (Figure 1B and S1D). After 75 minutes, the EGO was almost completely shaved off of the vacuole similarly to  $\Delta ego1$  strain (Figure 1C). TORC1 puncta formation tracked with EGO removal from the vacuolar membrane displayed twice more cells presenting TOROIDs after ~60 minutes of BPS treatment (Figure 1C, 1D and Figure S1D). Measurements from single-cell estimate the half-time of TOROID formation upon EGO depletion to be about 7 minutes (Figure 1E and 1F). Taken together, these data demonstrate that acute depletion of EGO from the vacuole is sufficient to induce TOROID formation.

To rapidly re-establish EGO signalling, we exploited the vacuole fusion that occurs during zygote formation <sup>39</sup>. Specifically, we crossed a *MATa*  $\Delta gtr1 \Delta gtr2$  strain, which constitutively displays a TOROID marked with GFP-Tor1, with a *MATa* partner containing Vph1-mCherry to delineate the vacuolar membrane (Figure 1G). As a control, we also used a *MATa*  $\Delta gtr1 \Delta gtr2$  *VPH1-mCherry* partner. After mixing of the mating partners, budding zygotes were staged as either early, intermediate, or late (Figure 1G). Early zygotes possessed a small bud and fragmented vacuoles that remained in the *MATa* parent. Intermediate zygotes possessed larger buds in which some Vph1-mCherry signal was observed. Late zygotes possessed a bud roughly the size of the parent cells and vacuole exchange between the parents in addition to the bud was observed. In crosses between  $\Delta gtr1 \Delta gtr2$  parents, a TOROID, initially present in the *MATa* parent, started to be also detected in about 50% of buds and some *MATa* parents, already at the intermediate zygote stage (Figure 1G, and 1H). This pattern was not observed in crosses with *MATa* *GTR1 GTR2 VPH1-mCherry*. In this case, TORC1 puncta were observed in only very few buds, and, at late stages even disappear from the *MATa* parent (Figure 1H). Live, single-cell imaging also demonstrated that TOROIDs from this mating dissolve promptly upon entry into the bud, upon mixing with vacuolar membrane possessing functional EGO (Figure 1I). The half-time to complete punctum dissolution was approximately 2.5 minutes (Figure 1J). These data indicate that acute loss or re-establishment of EGO activity, in the absence of potentially confounding inputs from other nutrient-regulated signalling pathways, is sufficient to trigger or dissolve TOROIDs, respectively. This supports the notion that the EGO regulates TOROID formation, potentially through direct physical interaction with TORC1 and/or TOROIDs.

## TOROIDs partially co-localize with EGO puncta

Previous work demonstrated that Gtr1/2 can physically interact with TORC1<sup>25,40</sup> and our results suggested that this interaction is necessary for regulating TOROID formation. To probe this idea, we assessed how the EGO and TORC1 localize with respect to one another. At the outset, we ensured that introduction of fluorescent tags did not compromise protein function. This was critical as we frequently encountered rapamycin hyper-sensitivity in singly, and especially doubly tagged strains that correlated with aberrant protein localizations. For example, using a GFP-Tor1, Ego3-3xmCherry strain, it has recently been shown that TORC1 and EGO co-localize in discrete puncta<sup>41,42</sup>. However, in this background there appears to be a synthetic interaction between these *TOR1* and *EGO3* alleles as TORC1 puncta are present even in glucose-replete conditions (Figure S2A). We noted similar, synthetic loss-of-function phenotypes between *GFP-TOR1* and *EGO3-mScarlet*, *EGO2-mScarlet*, and *EGO1-mCherry* (data not shown). Importantly, when assessed separately, both TORC1 (marked with GFP-Kog1) and the EGO (marked with *EGO3-GFP*) localized diffusely around the vacuole membrane in glucose-replete cells but collapsed into a punctum within 10 minutes of acute glucose depletion. Both puncta dissolved again within minutes of glucose replenishment (Figure 2A-B). We note that failure to appreciate the hypomorphic nature of tagged alleles may lead to incorrect conclusions and likely underlies discrepancies found in the literature.

A strain expressing GFP-Kog1 and Ego3-3xmCherry appeared to be relatively uncompromised with nearly *WT* levels of TOROIDs in glucose-replete and post-diauxic shift (PDS) cultures (Figure 2C and S2A). When these cells were cultured PDS, co-localization between TORC1 and EGO was moderate, as reflected by a Pearson's coefficient of 0.44 (Figure S2B). This co-localization also appeared to be asymmetric: while the EGO signal overlapped strongly with the TORC1 signal (Mander's coefficient (MC): 0.71; Figure S2B), the TORC1 signal overlap with the EGO signal was less robust (MC: 0.45; Figure S2B). Further characterization showed that small EGO puncta did not co-localize with the TORC1 signal (Pearson's coefficient (PC<sub><500nm</sub>): -0.004 ± 0.095; Figure S2C) while large EGO puncta did (PC<sub>>500nm</sub>: 0.525 ± 0.175). In contrast, large and small TORC1 puncta displayed similar overlaps with the EGO signal (PC<sub><500nm</sub>: 0.315 ± 0.023; PC<sub>>500nm</sub>: 0.361 ± 0.095; Figure S2C). Together, these data show that both EGO and TORC1 form condensates upon acute glucose depletion or in PDS cells, and that large EGO puncta seem to require a TOROID but not vice versa.

We next wished to characterize how guanine nucleotide loading status of the Gtrs affects EGO puncta formation. Although deletion of *GTR1* and *GTR2* promotes TORC1 puncta formation (Prouteau et al., 2017, Figure 1), EGO-TC puncta were absent in these strains (Figure 2D). Reintroduction of "active" *GTR* alleles (Gtr1<sup>GTP</sup>/Gtr2<sup>GDP</sup>) antagonized both TORC1 and EGO puncta formation regardless of the growth state while reintroduction of "inactive" *GTR* alleles (Gtr1<sup>GDP</sup>/Gtr2<sup>GTP</sup>) enhanced formation of TOROIDs but, curiously, not EGO puncta (Figure 2E-F). In  $\Delta gtr1 \Delta gtr2$  and Gtr1<sup>GDP</sup>/Gtr2<sup>GTP</sup> strains which contain TOROIDs, TORC1 activity is reduced as evidenced by their rapamycin hypersensitivity (Figure 2G). As a complementary means to assess the effects of nucleotide loading status of the Gtrs on EGO and TORC1 puncta formation we also used mutant strains in which Gtr GAP activities had been altered. Deletion of *IML1/SEA1*, which compromises SEACIT activity leading to Gtr1<sup>GTP</sup> accumulation, antagonized EGO and TORC1 puncta formation (Figure S2D-F). In contrast, deletion of *SEA3*, a

proposed SEACAT component, augmented EGO and TORC1 puncta formation (Figure S2D-F). Finally, deletion of *LST4* or *LST7*, which leads to Gtr2<sup>GTP</sup> accumulation, promoted EGO and TORC1 puncta formation (Figure S2D-F). Collectively, these results confirm and extend our previous observations<sup>27</sup> that the nucleotide loading status of the Gtrs dictate TOROID formation: whether generated by nutrient levels, mutations in the GAPs or mutations in the *GTRs* themselves, Gtr1<sup>GTP</sup>/Gtr2<sup>GDP</sup> antagonize, while Gtr1<sup>GDP</sup>/Gtr2<sup>GTP</sup> promote, TOROID formation. The EGO also forms a punctum, which in most, but not all cases, correlates with the presence of a TOROID, the notable exceptions being the lack of EGO puncta in  $\Delta gtr1 \Delta gtr2$  cells and in exponentially growing cells expressing “inactive” GTRs. These last results demonstrate that EGO puncta are not necessary for TOROID formation but can assemble with TOROIDS in a Gtr-dependent manner. In contrast, active EGO is needed to prevent TOROID formation.

Wishing to further characterize the molecular mechanism by which the EGO interacts with TORC1 to regulate its supramolecular organization we first performed *in vitro* binding assays between EGO variants and free TORC1 dimers purified from exponentially growing cells or TOROIDS from PDS cells. These assays demonstrated that purified “active” EGO interacts preferentially, albeit weakly, with TORC1 dimers (Figure 2H-I). In contrast, purified “inactive” EGO interacts robustly with TORC1 dimers and even more so with TOROIDS (Figure 2H-I). Thus, in contrast to the situation reported for mammalian cells<sup>21</sup>, in yeast, the EGO binds TORC1 regardless of which guanine nucleotides are bound to the Gtrs. This is consistent with prior genetic observations that the EGO can both positively and negatively regulate TORC1 activity<sup>25</sup>, see discussion).

## High resolution Cryo-EM TOROID Structure

To better understand the molecular regulation of TOROID (dis)assembly, we purified TORC1 from *KOG1-TAP  $\Delta tor1$*  cells grown PDS and acquired a high-resolution TOROID structure by cryo EM. We hypothesized that TOROIDS containing only Tor2, rather than a mix of Tor1 and Tor2, could yield a higher resolution structure. Initial attempts to determine the TOROID structure using helical reconstruction resulted in 3D reconstructions at rather low resolution (FSC<sub>0.143</sub>: 9.1 Å), despite the apparent high quality of the obtained data and ensuing 2D class averages (Figure 3A, Figure S3A-B). The relatively poor precision of helical symmetry determination on the un-symmetrized map (Figure S3A) suggested that instead of being a rigid helix, TOROID filaments resemble a flexible, slinky-like spring with varying pitch. Therefore, helical reconstruction most probably results in averaging out of TORC1 units along the helical assembly. To overcome this issue, we employed signal subtraction protocols<sup>43,44</sup>, using the known positions of TORC1 units in the helical reconstruction, to obtain a set of signal subtracted particles that could be further analyzed using a regular single particle analysis (SPA) pipeline (Figure S3A). We used a broad 3D mask including parts of neighboring TORC1 units surrounding a central TORC1 in the TOROID helix to ensure that information on the TORC1-TORC1' interfaces remained intact.

3D reconstruction using signal-subtracted TORC1 particles and employing D1 symmetry and non-uniform refinement in CryoSPARC<sup>45</sup> resulted in a 3.85 Å map according to the gold standard FSC=0.143 criterion, which enabled us to build a nearly complete structural model of yeast TORC1 in the TOROID (Figure 3B,

Figure S3A-C). While the final map displays heterogeneity in terms of resolution (Figure S3B-C), the symmetric nature of the TOROID assembly could be exploited to unambiguously build the majority of the TORC1 structure, with many regions showing density for amino acid side chains (Figure 3D). Moreover, it is apparent from the 3D reconstruction and local resolution estimation that the interactions between adjacent TORC1 units along the TOROID helix (intra-coil) are far more prominent than interactions along the helix z-direction (inter-coil; Figure 3A, S3B-C), which is also reflected by the resolution difference at the intra-coil and inter-coil interfaces.

The overall yeast TORC1 structure extracted from TOROIDs is very similar to its mammalian counterpart (mTORC1, Figure 4A), as shown by a structural alignment of individual Tor2/mTOR (Figure 4B), Kog1/RAPTOR (Figure 4C) and Lst8 subunits (Figure S4A, B). While yeast and human Lst8 are virtually identical (RMSD= 0.937 Å over 252 aligned main-chain atoms), the main differences between Tor2/mTOR (RMSD= 3.311 over 1608 aligned main-chain atoms) and Kog1/RAPTOR (RMSD= 2.371 over 866 aligned main-chain atoms), can be traced to a conformational difference of Tor2, and the presence of previously uncharacterized additional  $\alpha$ -helical regions for Kog1 (Figure 4B-C). We compared our structure of yeast TORC1 present in TOROIDs with structures of inactive mTORC1 and active mTORC1 bound to Rheb<sup>16</sup>. Tor2 in TORC1 in TOROIDs is structurally more similar to mTOR in inactive mTORC1 (RMSD<sub>inactive</sub>= 3.311 Å) than in Rheb bound mTORC1 (RMSD<sub>active</sub>= 10.388 Å; Figure 4B). Indeed, TORC1 in TOROIDs has an even more “open” conformation than inactive human mTORC1 (Figure 4A): the HORN region of Tor2 makes a 7° or 23° outward shift when compared to inactive or Rheb-bound mTORC1 respectively (Figure 4B).

Comparison of yeast Kog1 and human RAPTOR reveals a ‘Twix’ region contributed by two  $\alpha$ -helices connected by a poly-glutamine linker that is present in Kog1 but completely absent from human RAPTOR. Alignment of *S. cerevisiae* Kog1 with orthologous sequences from *H. sapiens*, *S. Pombe* and *C. thermophilum* indicated that the Twix is uniquely present in budding yeast (Figure S4C-D). The Twix region is situated between  $\alpha$ -helices 26 and 29 of Kog1 (Figure S4C-D), and interacts with the FRB’ domain of Tor2’ in an adjacent TORC1’ subunit with residues Gln2039, Asp2042 and Tyr2045 of Tor2’ respectively interacting with Glu865, Tyr829/Asn872 and Asn 876 of Kog1 (Figure 4D). Adjacent to the Twix region, we observed density for an  $\alpha$ -helix not directly connected to surrounding parts of the structure, yet in close proximity to Lys1016 of Kog1 which terminates  $\alpha$ -helix 34 (residues 1005 – 1016, Figure S4D). Careful inspection of the sequence succeeding Lys1016 and ensuing model building in Coot led to the identification of the region as being a helix with sequence ‘P<sub>1069</sub>MRTSLAKLFQSLGFSES<sub>1086</sub>’ (Figures 3D, 4D, S4E), which we termed the ‘Tack’ region. Sequence alignments demonstrated that this region precedes the sequence that aligns with the RAPTOR ‘Claw’ which was shown to interact with RagC in RAPTOR-Rag-Ragulator reconstructions<sup>22,23</sup>. In this vicinity, the structure displays a number of prominent molecular interactions leading to a robust TORC1-TORC1’ binding interface that we term the hub of interactions. Phe1083 and Ser1086, at the very tip of the Tack  $\alpha$ -helix, make Van der Waals interactions with Pro2201 of the KD’ region of Tor2’ and Arg884’ of Kog1’ respectively (Figure 4D). Adjacent to Pro2201, Trp2207 sits in between Arg884, Lys885 and Arg888 of Kog1, forming a prominent

cation- $\pi$  interaction with Arg884 situated near the tip of the Tack  $\alpha$ -helix and the base of the Twix region (Figure 4D). The Twix and the Tack shield the kinase active site and thereby block substrate access, providing, together with the large allosteric change described above, a structural explanation for why TORC1 in TOROIDs is inactive (Figure 4D, Figure S4C).

## Mutations confirm observed TORC1/TORC1' interfaces

To interrogate the structural insights obtained from the observed interfaces, we selected sets of residues in the inter- and intra-coil interfaces for mutation using CrispR/Cas9 (Figure 5A-B and S5). The impact of these mutations was assessed by determining the relative size of TORC1 puncta in cells grown PDS (Figure S5E). In parallel, all mutants were tested in spot assays on rapamycin plates to identify mutations that compromise TORC1 activity (Figure S5F). In these analyses, we first assessed what we considered to be control mutations – mutation of exposed residues in the vicinity of the intra- and inter-coil interfaces, but not obviously engaged in TORC1-TORC1' interactions. As expected, these mutations (Kog1<sup>K1383A</sup> and Kog1 <sup>$\Delta$ 1544-end</sup>) did not significantly affect TOROID size or rapamycin sensitivity (Figure S5A, C and F). In contrast, mutation of W1279 of Tor1, which is not predicted to mediate contacts within the helix but is predicted to be important to stabilize the FAT domain, yielded a reduction in TOROID size as well as rapamycin hypersensitivity, consistent with a loss of TORC1 particle integrity (Figure S5A, C and F).

Inter-coil interactions, although clearly visible in the helical reconstruction, appear almost completely absent in the signal subtracted map, and only become apparent when using a higher contour threshold level during visualization. Based on our helical reconstruction, the inter-coil interface is predominantly formed between the Tor2 HORN and the Kog1' WD domain (Figure 3). To validate this, two exposed loops in the HORN, Tor2<sup>337-345</sup> (Tor1<sup>326-334</sup>) and Tor2<sup>379-381</sup> (Tor1<sup>368-370</sup>), were substituted by poly alanine-glycine stretches. These strains displayed a significant reduction in TOROID size as well as an increase in rapamycin resistance (Figure S5B and S5D-F). An additional protruding region of the Tor2 kinase domain also appeared to interact with Kog1'. Although attempts to generate mutations in this region of Tor2 were unsuccessful, mutation of the equivalent region of Tor1 (Tor1<sup>1449/54/56A</sup>) similarly resulted in a reduced TOROID size and increased rapamycin resistance (Figure S5B and S5D-F).

Given the higher resolution of this region in the signal subtracted map, amino acids involved in intra-coil interactions were easier to trace (Figure 5 and S5A, S5C and S5E-F). Intra-coil interactions are plentiful, and mainly contributed by Kog1 interacting with Kog1', Lst8', and the KD' and FAT' regions of Tor2' from an adjacent TORC1' unit. Glu784 and Ser896 of Kog1 interacts with His292 of Lst8' and alanine substitution of this His reduces TOROID formation (Lst8<sup>H292A</sup>; Figure 5A-B). Similar results were obtained with reciprocal mutations in Kog1 (Kog1<sup>E784A</sup>, Kog1<sup>S895-896A</sup> Figure 5A-B and S5E-F). The backbone carbonyl oxygen of Gly781 in Kog1 interacts with Gln29 of Lst8' and alanine substitution of this Gln residue strongly reduces TOROID formation and leads to a significant increase in Rapamycin resistance (Figure S5A, S5C and S5E-F).

Striking amongst the intra-coil interactions, and as alluded to above, is the TORC1-TORC1' hub of interactions, formed through extensive contacts between Kog1 and Tor2'. These contacts include interactions between the Twix helices of Kog1 and the FRB domain of Tor2' (Figure S4C-D), the tip of the Tack helix of Kog1 and the KD of Tor2' (Figure 4D, S4C and 5), and a basic pocket of Kog1 that hosts Trp2207 from the Lst8 Binding Element (LBE) of Tor2'. The apparent cation-pi interaction between Tor2<sup>W2207</sup> and Kog1<sup>R884</sup> where particularly intriguing as mutations in the corresponding residues of mTOR and RAPTOR (mTOR<sup>R2266P</sup> and Raptor<sup>D635N</sup>) have been identified in human carcinomas (<https://cancer.sanger.ac.uk/cosmic>). To test if this cation-pi interaction is important for TORC1 regulation, we assessed the consequences of combined mutations of Trp2207 of Tor2 and the analogous site in Tor1 (Tor1<sup>W2203R</sup>, Tor2<sup>W2207R</sup>), anticipating to create a charge repulsion with Kog1'. Consistently, in this strain, TOROID formation was absent (Figure 5C and S5E), and TORC1 was hyperactive as shown by increased rapamycin resistance (Figure S5F). We attempted to rescue these phenotypes by reverting Arg884 of Kog1 to Asp, the corresponding amino acid found in RAPTOR. However, *KOG1<sup>R884D</sup>* neither blocked TOROID formation on its own, nor did it rescue the increased rapamycin resistance and lack of TOROIDs of *TOR1<sup>W2203R</sup> TOR2<sup>W2207R</sup>* cells (data not shown), perhaps owing to the remaining positively charged residues surrounding Arg884 (see below). The potential significance of these cancer associated mutations is discussed below.

TOROID-like structures have not been reported in other systems, including mammals and we wondered if the yeast-specific Twix helices of Kog1 might be a reason why. To test if the Twix region is necessary for TOROID formation, and considering the poor local sequence conservation, we initially, and rather conservatively, replaced a region from  $\alpha$ 26 to  $\alpha$ 29 (including the Twix helices:  $\alpha$ 27  $\alpha$ 28), with the corresponding, smaller region of human Raptor to generate an allele that we named *kog1 Humanized Chimera* (*kog1<sup>HC</sup>*; Figure 5C). Cells expressing this allele of *KOG1* cultured PDS formed TOROIDs indistinguishably from *WT* cells (Figure 5B, C and S5E) suggesting that the Twix region is not required for TOROID formation (see also below).

### *kog1<sup>HC</sup>* allele unveils the TORC1/EGOC interaction domain

The *kog1<sup>HC</sup>* allele also replaces helix  $\alpha$ 29 of yeast Kog1 which contains the three basic residues (Kog1<sup>R884</sup>, Kog1<sup>K885</sup> and Kog1<sup>R888</sup>) thought to interact with Trp2207 of Tor2 with the equivalent helix  $\alpha$ 29 of Raptor which contains acidic amino acids instead of these arginines (Figure S4D). Although *KOG1<sup>R884D</sup>* did not suppress the inability of *TOR1<sup>W2203R</sup> TOR2<sup>W2207R</sup>* cells to form TOROIDs we wondered if *kog1<sup>HC</sup>* might. Indeed, we found this to be the case (Figure S5E) but, as presented below, not necessarily through charge complementation of Tor1<sup>W2203R</sup> Tor2<sup>W2207R</sup>.

As expected, the *TOR1<sup>W2203R</sup> TOR2<sup>W2207R</sup> kog1<sup>HC</sup>* strain presented a strong reduction in rapamycin resistance compared to the *TOR1<sup>W2203R</sup> TOR2<sup>W2207R</sup>* strain (Figure S5F). However, we unexpectedly noticed that *kog1<sup>HC</sup>* cells displayed hypersensitivity to rapamycin, to a level comparable to  $\Delta$ *gtr1*  $\Delta$ *gtr2* cells (Figure S5F). One explanation for the rapamycin hypersensitivity of *kog1<sup>HC</sup>* cells would be if they,

like  $\Delta gtr1 \Delta gtr2$  cells, constitutively from TOROIDs even in the presence of glucose. Thus, we decided to re-assess TORC1 localization in  $kog1^{HC}$  cells, as well as in all of the other mutant strains that we had created, in glucose-replete conditions. Amongst all of these strains, the  $kog1^{HC}$  strain alone displayed TOROIDs in glucose-replete conditions similarly to  $\Delta gtr1 \Delta gtr2$  cells (Figure 6A-D and data not shown).

Guessing that these phenotypes might be due to the human sequences (helices  $\alpha 28$  and/or  $\alpha 29$  of Raptor) that were introduced during the construction of  $kog1^{HC}$ , we generated a new  $kog1$  allele in which the Twix helices  $\alpha 27$  and  $\alpha 28$  of Kog1 were “cleanly” replaced with a short (AG)<sub>4</sub> linker (Figure 6A). We named this allele,  $kog1^{\Delta Twix}$ .  $kog1^{\Delta Twix}$ , like  $kog1^{HC}$ , formed TOROIDs normally when cells were cultured PDS (Figure 6B), but, unlike  $kog1^{HC}$ , do not form TOROIDs in exponential phase and displayed nearly normal sensitivity to rapamycin (Figure 6C). These observations confirm that the Twix helices are not a prerequisite for TOROID formation or normal TORC1 activity but that Kog1 helix  $\alpha 26$  and/or  $\alpha 29$  is important for basal TORC1 activity in a manner that cannot be complemented by the corresponding Raptor sequence.

We hypothesized that the phenotypes observed in the  $kog1^{HC}$  strain could be explained if TORC1 in these cells was unable to engage the EGOC. Several additional observations support this model. Similarly to  $\Delta gtr1 \Delta gtr2$  cells, in  $kog1^{HC}$  cells, EGOC puncta were not observed (Figure 6D-E), and TORC1 activity, as assessed by Sch9 phosphorylation, was reduced and largely insensitive to acute changes in glucose levels (Figure 6G). Furthermore, in pulldown experiments, unlike WT TORC1, TORC1 containing Kog1<sup>HC</sup> failed to robustly interact with purified EGOC (Figure 6H-I, S6A). Collectively, these results suggest that a key binding site for EGOC lies within helix  $\alpha 26$  and/or  $\alpha 29$  of Kog1, i.e. within the TOROID hub of interactions. They also demonstrate that TOROID assembly is necessary, but not sufficient for EGOC puncta formation (see Figure 2E, F; cells expressing inactive Gtr1<sup>GDP</sup>/Gtr2<sup>GTP</sup>, do not efficiently form EGOC puncta in glucose-replete conditions despite the presence of TOROIDs).

Based on these observations we wondered if  $kog1^{HC}$  suppressed the inability of  $TOR1^{W2203R} TOR2^{W2207R}$  cells to form TOROIDs because of its own inability to bind the EGOC rather than, or in addition to, charge complementation. Consistent with this idea we observed that the  $\Delta gtr1 \Delta gtr2$  double deletion was epistatic to  $TOR1^{W2203R} TOR2^{W2207R}$ :  $\Delta gtr1 \Delta gtr2 TOR1^{W2203R} TOR2^{W2207R}$  cells presented constitutive TOROIDs (Figure S6B). The implications of this observation are discussed below.

### **CrispR-based random mutagenesis confirms that the EGOC-TORC1 interaction interface overlaps with the TORC1-TORC1' hub of interactions**

Using the strains generated thus far, we observed a strong anti-correlation between TOROID size in PDS and rapamycin sensitivity (Pearson=-0.75; Figure S6C). Mutations compromising TORC1-TORC1' interactions have small TOROIDs and are resistant to rapamycin while mutations abrogating TORC1-EGOC binding have large TOROIDs and are sensitive to rapamycin. Thus it appears that sensitivity to rapamycin depends on the proportion of free and active TORC1 dimers (Figure S6C). Exploited this idea we set up a CrispR-based PCR random mutagenesis screen to further define the TORC1-EGOC interface. A

portion of the ARM domain of Kog1 surrounding  $\alpha$ 26 -  $\alpha$ 29 (residues 696-922) was chosen for mutagenesis (Figure 7A). The first selection step was rapamycin-hypersensitivity, expecting that mutants of interest would present a hypersensitive phenotype similar to  $\Delta gtr1/2$  and  $kog1^{HC}$  strains. The second step was to select for TOROID formation in glucose-replete cultures. A total of 3500 mutants were screened on 2.5 and 4 nM rapamycin plates. While the latter concentration appeared to be too stringent, selection with 2.5 nM rapamycin yielded 42, rapamycin-sensitive clones. Among these, 13 presented TOROIDs in glucose-replete media and these were retained and sequenced (Figure 7A and S7A-D). 17-point mutations were identified, of which 7 (marked in bold below) were the only mutation present in the clone and could thus be deemed causative (Figure 7B, S7B-D). Remarkably, while the Twix-encoding region was included in this screen, no mutation within this sequence was recovered, supporting the idea that it does not participate in EGOC-dependent regulation of TOROIDs.

Several mutations, alone (**bold**) or in combination, altered leucine residues involved in hydrophobic interactions between  $\alpha$ -helices (**L762P**, L765P, **L766P**, **L900P**, **L912Q**; Figure 7B and S7C-D) suggesting that local perturbation of domain packing may affect EGOC binding. L737Q (found in combination with L762P), at the junction of  $\alpha$ 21-22 helices, **C777R** and M778T in helix  $\alpha$ 24, **I802N** and **A804E** in helix  $\alpha$ 26, and I891N in helix  $\alpha$ 29 were recovered (Figure 7B and S7B-D) and we note that many of these map to a region which in Raptor is important for interaction with RagA (Raptor residues N557, C594 and 634-36; Figure 7B and alignment Figure S4D);<sup>23</sup>). Building on this observation we found that Kog1 helix  $\alpha$ 21 (which corresponds to  $\alpha$ 23 in Raptor, known to be important for RagA binding) is essential for proper TOROID dynamics since its substitution to an Alanine-Glycine stretch triggers constitutive TOROID formation (Figure 7C). Finally, we found that purified TORC1 harboring Kog1<sup>C777R</sup> or AG-substituted Kog1 helix  $\alpha$ 21 respectively presented much reduced or no EGOC binding activity (Figure 7D). Thus, Kog1 appears to interact with the GTRs similarly to how Raptor interacts with the RAGs.

Remarkably, the Tack helix appears to correspond to the Claw helical fragment of Raptor described to interact with RagC. To probe the importance of the Tack helix in TOROID regulation we made three poly AG substitutions. Replacement of the proximal  $\alpha$ -helix 34 (Kog1<sup>1004-1022</sup>) had no effect on TOROID regulation, while replacement of the entire Tack helix (Kog1<sup>1121-1131</sup>) leads to a mild, but significant, impairment of TOROID formation (Figure S7E, F). Replacement of the putative yeast Claw sequence (Kog1<sup>1121-1131</sup>;<sup>23</sup> presented no significant effect on either TOROID formation or regulation (Figure S7E-F), whereas equivalent mutations in Raptor prevent Rag-binding<sup>23</sup> which we predict would lead to constitutive TOROID formation. From these observations we conclude that, although similarly localized, the Tack helix does not function equivalently to the Raptor Claw. Instead, it provides structural elements (Kog1<sup>F1083</sup> binding to Tor2<sup>P2201</sup>) needed to stabilize the TOROID.

Based on these collective observations, we propose that, analogous to the binding observed in mammalian cells, EGOC binds to helices  $\alpha$ 21,  $\alpha$ 24,  $\alpha$ 26 and  $\alpha$ 29 of Kog1. This binding (Figure 7G) competes with a critical interface needed for TOROID formation, and would thus release/sequester free TORC1 dimers that are competent to signal to downstream effectors.

## Discussion

We previously reported<sup>27</sup> that glucose withdrawal triggers a rapid, Gtr1/2-dependent reorganization of TORC1 from a disperse localization over the surface of the vacuole to a hollow helical assembly that we named a TOROID. Our, at this time, low-resolution, 3D reconstruction revealed that TOROID-sequestered TORC1 is inactive due, at least in part, to rapamycin-FKBP12-like occlusion of the kinase active site. This unexpected mechanism underlying TORC1 regulation differs from the widely accepted model of mammalian TORC1 regulation and raised some important questions, some of which we have addressed in the present study.

We show here that the EGOc alone is sufficient to regulate TORC1/TOROID dynamics. Although we conclude that EGOc-mediated TOROID formation represents an important mechanism for the cell to regulate TORC1 signaling output, we do not wish to imply that this is the only mechanism through which glucose or other stimuli regulate TORC1. Indeed, in the absence of TORC1-EGOC interactions (e.g.  $\Delta gtr1 \Delta gtr2$  or  $kog1^{HC}$  cells) TORC1 is still partially regulated by glucose withdrawal/repletion (Figure 6G,<sup>27</sup>) and by osmotic shock (data not shown). This clearly indicates the existence of EGOc-independent TORC1 regulators. How such regulators (e.g. Snf1 and Pib2<sup>46,47</sup>) interface with TORC1/TOROID-based regulation remains an important unknown. The observation that some TORC1 activity remains in  $\Delta gtr1 \Delta gtr2$  cells – and mTORC1 activity in  $ragA ragB ragC ragD$  cells<sup>48</sup> – implies that not all TORC1 is sequestered into TOROIDs in this genetic background. Indeed, we favor a model in which there is a dynamic equilibrium between active, free TORC2 dimers and inactive TOROID polymers in a cell. Mutations or stimuli that shift the equilibrium towards free dimers would stimulate TORC1 signaling output, and vice versa. This hypothesis is supported by the strong anti-correlation that we see between TORC1 puncta size and rapamycin resistance (Supplementary Figure 6B). In such a model, one could envision that non-EGOC TORC1 regulators independently act on the pool of free TORC1 dimers. Additionally, distinct pools of TORC1 (e.g. endosomal TORC1;<sup>26</sup>) could be subjected to distinct upstream regulatory mechanisms.

The major advance of our present work, however, is the molecular insights we provide to explain how binding of EGOc liberates free TORC1 from TOROID polymers. Our new, high-resolution TORC1 map reveals that TOROIDs are rather spring-like with loose inter-coil interactions and robust intra-coil interactions. The weak inter-coil interactions bestow flexibility upon the TOROID structure for an as of yet unknown purpose. In contrast, the strong intra-coil interactions serve to occlude access to the active site, which, together with allosteric changes to the catalytic spine, ensures that TOROID-associated TORC1 is inactive. Closer inspection of the TORC1-TORC1' interface proximal to the kinase active site revealed an intriguing hub of interactions primarily involving Kog1 and Tor2'. Within this hub lies the budding-yeast-specific Twix helices (Kog1  $\alpha 27$  and  $\alpha 28$ ), that we posited might underlie TOROID formation which, to date, has also only been observed in budding yeast. While performing experiments from which we ultimately concluded that the Twix *per se* does not play an essential role in TOROID formation, we discovered that the region flanking the Twix does. Specifically, using a CrispR/cas9-supported random mutagenesis screen, we found that  $\alpha$ -helices 21-26 and 29 of Kog1 serve as a binding platform for Gtr1

and Gtr2 of the EGO. This observation was satisfying but not obvious: satisfying because the corresponding region of Raptor ( $\alpha 23$ -  $\alpha 29$ ) was previously found to bind to RagA and RagC (Rogala et al., 2019); not obvious because the positioning of the Twix helices should occlude GTPase binding. We hypothesize that the Twix helices are flexible - potentially more so at the TOROID termini - and that they are displaced upon EGO binding. The molecular details of this displacement await a TORC1-EGO structure. Nevertheless, these observations clearly demonstrate that EGO binding to this region of Kog1 disrupts the hub of interactions needed to sustain TOROID assembly, providing a mechanism to explain how the EGO can liberate and/or maintain free, active TORC1 dimers – the major conclusion of this paper.

Although this model of TORC1 regulation is appealing, it is oversimplified, as it does not take into account the nucleotide loading status of Gtr1 and Gtr2. *A priori*, one could posit that only “active” EGO binds TORC1, preventing its association into a TOROID. However, compelling evidence suggests that inactive EGO also binds TORC1:

i/ In *in vitro* pulldowns we observe that TORC1 interacts with “inactive” EGO even more robustly than “active” EGO (Figure 2H).

ii/ Expression of “inactive” *gtr* alleles produce phenotypes that are more severe than simple *gtr1/2* deletion<sup>25</sup>. Consistently, deletion of *LST4* or *LST7* (Subunits of the Gtr2 GAP; *LST* = Lethal with Sec Thirteen) shows synthetic lethality with hypomorphic alleles of *sec13*<sup>49</sup> which encodes a SEACAT component.

iii/ “Inactive” EGO partially colocalizes with TOROIDS (Figure S2).

The RAG GTPases do not solely interact with TORC1; they also interact with their respective GAPs. Interestingly, recent evidence suggests that with both GATOR1 and Folliculin-Fnip, the RAGs have multiple binding modes<sup>18,50,51</sup>. Based on this previous literature and the arguments presented above, we speculate that the EGO may also have multiple TORC1-interaction modes.

Is mammalian TOR similarly regulated via a TOROID like structure? We do not yet have an answer for this important question. As far as we are aware, comparison of yeast and mammalian TORC1 structures does not present any obvious structural argument to preclude the existence of a mammalian TOROID.

mTORC1 resides on lysosomes, which range in diameter from 0.1 to 1  $\mu\text{m}$ <sup>52</sup>. In contrast, a yeast vacuole is around 2 – 3  $\mu\text{m}$  in diameter. Thus, there are likely far fewer mTORC1s per lysosome compared to the 500-1000 yeast TORC1s per vacuole. This implies that if mTOROIDS do exist their appearance by light microscopy would be far less striking than what we observe in yeast. Furthermore, the mTOR field almost exclusively uses a single antibody - Cell Signaling 7C10 – for IHC studies of mTOR. This antibody recognizes a phospho-epitope that may not be accessible or even present in a putative mTOROID helix. Thus, it is very possible that mTORC1 in mTOROIDS would not be visible using this reagent. We note that the RagA<sup>GDP</sup> RagC<sup>GTP</sup> conformation of the RAGs, often considered to be inactive, in some studies has

been shown to potently inhibit mTORC1 function<sup>53</sup>. This observation is not consistent with the current model that active RAGs simply recruit mTORC1 to the lysosome for subsequent activation by Rheb. In conclusion, we believe that it is not yet appropriate to rule out the existence of mTOROIDs.

The presence of mTOROIDs could explain why mTOR<sup>R2266P</sup>, and possibly Raptor<sup>D635N</sup>, are associated with carcinoma based on our finding that substitution of the analogous residue in Tor1<sup>W2203R</sup> Tor2<sup>W2207R</sup> generated cells that did not form TOROIDs and appeared to possess hyperactive TORC1 signaling (i.e. were resistant to rapamycin). This double mutant is intriguing as it still requires the Gtrs to prevent TOROID formation. Perhaps this mutant can use the binding of “inactive” EGOc to prevent TOROID formation. Alternatively, the mutant may possess a higher affinity for low levels of “active” EGOc in PDS cells. Further characterization of this mutant is clearly warranted.

## Declarations

### ACKNOWLEDGMENTS

R.L. acknowledges support from the Canton of Geneva, the Swiss National Science Foundation, SNF Sinergia METEORIC, the Swiss National Centre for Competence in Research Chemical Biology and the European Research Council AdG TENDO. I.G. is supported by the European Union’s Horizon 2020 research and innovation programme under grant agreement No 647784 to IG. S.N.S. is supported by the Flanders Institute for Biotechnology (VIB). J.F. was supported by a long-term European Molecular Biology Organization (EMBO) fellowship (ALTF441-2017) and a Marie Skłodowska-Curie actions individual fellowship (789385, RespViRALI). Support and use of iNEXT resources, the cryo-electron microscopy (cryo-EM) service platform at EMBL Heidelberg and CryoGENic facility (DCI Geneva) is acknowledged. J.F. and A.D. acknowledge the use of the Grenoble IBS-EMBL computer cluster and the technical assistance of Aymeric Peuch.

### AUTHOR CONTRIBUTIONS

Genetic engineering and cellular biology experiments were carried out by M.P., C.B., L.B. and R.L. EGOc expression and purification were performed by C.G. and TOROID purifications, pull downs and cryo-EM grid preparations were performed by M.P. and C.B. EM data collection were performed by M.P., C.B., J.F. and A.D. Cryo-EM data processing, model building and refinement were carried out by J.F. and A.D. with additional input from Y.S. Experimental design was conducted by M.P., C.B., J.F., I.G., A.D. and R.L. The first draft of the manuscript was written by M.P., C.B., J.F. and R.L. with inputs from all authors.

### DECLARATION OF INTERESTS

The authors declare no conflicts of interest.

## References

1. Keith, C.T. & Schreiber, S.L. PIK-related kinases: DNA repair, recombination, and cell cycle checkpoints. *Science* **270**, 50–1 (1995).
2. Tatebe, H. & Shiozaki, K. Evolutionary Conservation of the Components in the TOR Signaling Pathways. *Biomolecules* **7**(2017).
3. Gaubitz, C., Prouteau, M., Kusmider, B. & Loewith, R. TORC2 Structure and Function. *Trends Biochem Sci* **41**, 532–545 (2016).
4. Riggi, M. et al. Decrease in plasma membrane tension triggers PtdIns(4,5)P-2 phase separation to inactivate TORC2. *Nature Cell Biology* **20**, 1043+ (2018).
5. Eltschinger, S. & Loewith, R. TOR Complexes and the Maintenance of Cellular Homeostasis. *Trends in Cell Biology* **26**, 148–159 (2016).
6. Loewith, R. et al. Two TOR complexes, only one of which is rapamycin sensitive, have distinct roles in cell growth control. *Mol Cell* **10**, 457–68 (2002).
7. Reinke, A. et al. TOR complex 1 includes a novel component, Tco89p (YPL180w), and cooperates with Ssd1p to maintain cellular integrity in *Saccharomyces cerevisiae*. *J Biol Chem* **279**, 14752–62 (2004).
8. Urban, J. et al. Sch9 is a major target of TORC1 in *Saccharomyces cerevisiae*. *Mol Cell* **26**, 663–74 (2007).
9. Huber, A. et al. Characterization of the rapamycin-sensitive phosphoproteome reveals that Sch9 is a central coordinator of protein synthesis. *Genes Dev* **23**, 1929–43 (2009).
10. Kamada, Y. et al. Tor-mediated induction of autophagy via an Apg1 protein kinase complex. *J Cell Biol* **150**, 1507–13 (2000).
11. MacGurn, J.A., Hsu, P.C., Smolka, M.B. & Emr, S.D. TORC1 regulates endocytosis via Npr1-mediated phosphoinhibition of a ubiquitin ligase adaptor. *Cell* **147**, 1104–17 (2011).
12. Zimmermann, C. et al. TORC1 Inhibits GSK3-Mediated Elo2 Phosphorylation to Regulate Very Long Chain Fatty Acid Synthesis and Autophagy. *Cell Rep* **18**, 2073–2074 (2017).
13. Liu, G.Y. & Sabatini, D.M. mTOR at the nexus of nutrition, growth, ageing and disease. *Nat Rev Mol Cell Biol* **21**, 183–203 (2020).
14. Aylett, C.H. et al. Architecture of human mTOR complex 1. *Science* **351**, 48–52 (2016).
15. Baretic, D., Berndt, A., Ohashi, Y., Johnson, C.M. & Williams, R.L. Tor forms a dimer through an N-terminal helical solenoid with a complex topology. *Nat Commun* **7**, 11016 (2016).
16. Yang, H. et al. Mechanisms of mTORC1 activation by RHEB and inhibition by PRAS40. *Nature* **552**, 368–373 (2017).
17. Shen, K., Choe, A. & Sabatini, D.M. Intersubunit Crosstalk in the Rag GTPase Heterodimer Enables mTORC1 to Respond Rapidly to Amino Acid Availability. *Molecular Cell* **68**, 552+ (2017).
18. Shen, K. & Sabatini, D.M. Ragulator and SLC38A9 activate the Rag GTPases through noncanonical GEF mechanisms. *Proc Natl Acad Sci U S A* **115**, 9545–9550 (2018).
19. Kim, J. & Kim, E. Rag GTPase in amino acid signaling. *Amino Acids* **48**, 915–928 (2016).

20. Nada, S. et al. The novel lipid raft adaptor p18 controls endosome dynamics by anchoring the MEK-ERK pathway to late endosomes. *EMBO J* **28**, 477–89 (2009).
21. Sancak, Y. et al. Ragulator-Rag complex targets mTORC1 to the lysosomal surface and is necessary for its activation by amino acids. *Cell* **141**, 290–303 (2010).
22. Anandapadamanaban, M. et al. Architecture of human Rag GTPase heterodimers and their complex with mTORC1. *Science* **366**, 203–210 (2019).
23. Rogala, K.B. et al. Structural basis for the docking of mTORC1 on the lysosomal surface. *Science* **366**, 468–475 (2019).
24. Morozumi, Y. & Shiozaki, K. Conserved and Divergent Mechanisms That Control TORC1 in Yeasts and Mammals. *Genes (Basel)* **12**(2021).
25. Binda, M. et al. The Vam6 GEF controls TORC1 by activating the EGO complex. *Mol Cell* **35**, 563–73 (2009).
26. Hatakeyama, R. et al. Spatially Distinct Pools of TORC1 Balance Protein Homeostasis. *Mol Cell* **73**, 325-338 e8 (2019).
27. Prouteau, M. et al. TORC1 organized in inhibited domains (TOROIDs) regulate TORC1 activity. *Nature* **550**, 265–269 (2017).
28. Zhang, T. et al. Structural insights into the EGO-TC-mediated membrane tethering of the TORC1-regulatory Rag GTPases. *Sci Adv* **5**, eaax8164 (2019).
29. Gao, M. & Kaiser, C.A. A conserved GTPase-containing complex is required for intracellular sorting of the general amino-acid permease in yeast. *Nat Cell Biol* **8**, 657–67 (2006).
30. Peli-Gulli, M.P., Sardu, A., Panchaud, N., Raucchi, S. & De Virgilio, C. Amino Acids Stimulate TORC1 through Lst4-Lst7, a GTPase-Activating Protein Complex for the Rag Family GTPase Gtr2. *Cell Rep* **13**, 1–7 (2015).
31. Powis, K. & De Virgilio, C. Conserved regulators of Rag GTPases orchestrate amino acid-dependent TORC1 signaling. *Cell Discov* **2**, 15049 (2016).
32. Sekiguchi, T., Hirose, E., Nakashima, N., Ii, M. & Nishimoto, T. Novel G proteins, Rag C and Rag D, interact with GTP-binding proteins, Rag A and Rag B. *J Biol Chem* **276**, 7246–57 (2001).
33. Broach, J.R. Nutritional Control of Growth and Development in Yeast. *Genetics* **192**, 73–105 (2012).
34. Dechant, R., Saad, S., Ibanez, A.J. & Peter, M. Cytosolic pH regulates cell growth through distinct GTPases, Arf1 and Gtr1, to promote Ras/PKA and TORC1 activity. *Mol Cell* **55**, 409–21 (2014).
35. Sullivan, A., Wallace, R.L., Wellington, R., Luo, X. & Capaldi, A.P. Multilayered regulation of TORC1-body formation in budding yeast. *Mol Biol Cell* **30**, 400–410 (2019).
36. Gao, X.D., Wang, J., Keppler-Ross, S. & Dean, N. ERS1 encodes a functional homologue of the human lysosomal cystine transporter. *FEBS J* **272**, 2497–511 (2005).
37. Prouteau, M., Daugeron, M.C. & Seraphin, B. Regulation of ARE transcript 3' end processing by the yeast Cth2 mRNA decay factor. *EMBO J* **27**, 2966–76 (2008).

38. Dubouloz, F., Deloche, O., Wanke, V., Cameroni, E. & De Virgilio, C. The TOR and EGO protein complexes orchestrate microautophagy in yeast. *Mol Cell* **19**, 15–26 (2005).
39. Weisman, L.S. Organelles on the move: insights from yeast vacuole inheritance. *Nat Rev Mol Cell Biol* **7**, 243–52 (2006).
40. Kira, S. et al. Reciprocal conversion of Gtr1 and Gtr2 nucleotide-binding states by Npr2-Npr3 inactivates TORC1 and induces autophagy. *Autophagy* **10**, 1565–78 (2014).
41. Kira, S. et al. Dynamic relocation of the TORC1-Gtr1/2-Ego1/2/3 complex is regulated by Gtr1 and Gtr2. *Mol Biol Cell* **27**, 382–96 (2016).
42. Ukai, H. et al. Gtr/Ego-independent TORC1 activation is achieved through a glutamine-sensitive interaction with Pib2 on the vacuolar membrane. *PLoS Genet* **14**, e1007334 (2018).
43. de la Rosa-Trevin, J.M. et al. Scipion: A software framework toward integration, reproducibility and validation in 3D electron microscopy. *Journal of Structural Biology* **195**, 93–99 (2016).
44. Ilca, S.L. et al. Localized reconstruction of subunits from electron cryomicroscopy images of macromolecular complexes. *Nature Communications* **6**(2015).
45. Punjani, A., Zhang, H.W. & Fleet, D.J. Non-uniform refinement: adaptive regularization improves single-particle cryo-EM reconstruction. *Nature Methods* **17**, 1214+ (2020).
46. Hughes Hallett, J.E., Luo, X. & Capaldi, A.P. Snf1/AMPK promotes the formation of Kog1/Raptor-bodies to increase the activation threshold of TORC1 in budding yeast. *Elife* **4**(2015).
47. Tanigawa, M. et al. A glutamine sensor that directly activates TORC1. *Communications Biology* **4**(2021).
48. Lawrence, R.E. et al. A nutrient-induced affinity switch controls mTORC1 activation by its Rag GTPase-Ragulator lysosomal scaffold. *Nat Cell Biol* **20**, 1052–1063 (2018).
49. Roberg, K.J., Bickel, S., Rowley, N. & Kaiser, C.A. Control of amino acid permease sorting in the late secretory pathway of *Saccharomyces cerevisiae* by SEC13, LST4, LST7 and LST8. *Genetics* **147**, 1569–1584 (1997).
50. Shen, K. et al. Cryo-EM Structure of the Human FLCN-FNIP2-Rag-Ragulator Complex. *Cell* **179**, 1319–1329 e8 (2019).
51. Lawrence, R.E. et al. Structural mechanism of a Rag GTPase activation checkpoint by the lysosomal folliculin complex. *Science* **366**, 971–977 (2019).
52. Novikoff, A.B., Beaufay, H. & De Duve, C. Electron microscopy of lysosomeric fractions from rat liver. *J Biophys Biochem Cytol* **2**, 179–84 (1956).
53. Yang, S. et al. The Rag GTPase Regulates the Dynamic Behavior of TSC Downstream of Both Amino Acid and Growth Factor Restriction. *Developmental Cell* **55**, 272+ (2020).
54. Gibson, D.G. Synthesis of DNA fragments in yeast by one-step assembly of overlapping oligonucleotides. *Nucleic Acids Res* **37**, 6984–90 (2009).
55. Laughery, M.F. et al. New vectors for simple and streamlined CRISPR-Cas9 genome editing in *Saccharomyces cerevisiae*. *Yeast* **32**, 711–20 (2015).

56. Guichard, P., Hamel, V., Neves, A. & Gonczy, P. Isolation, cryotomography, and three-dimensional reconstruction of centrioles. *Centrosome & Centriole* **129**, 191–209 (2015).
57. Zheng, S.Q. et al. MotionCor2: anisotropic correction of beam-induced motion for improved cryo-electron microscopy. *Nature Methods* **14**, 331–332 (2017).
58. Rohou, A. & Grigorieff, N. CTFFIND4: Fast and accurate defocus estimation from electron micrographs. *Journal of Structural Biology* **192**, 216–221 (2015).
59. Tang, G. et al. EMAN2: An extensible image processing suite for electron microscopy. *Journal of Structural Biology* **157**, 38–46 (2007).
60. Scheres, S.H. RELION: implementation of a Bayesian approach to cryo-EM structure determination. *J Struct Biol* **180**, 519–30 (2012).
61. Zhang, K. Gctf: Real-time CTF determination and correction. *Journal of Structural Biology* **193**, 1–12 (2016).
62. Rosenthal, P.B. & Henderson, R. Optimal determination of particle orientation, absolute hand, and contrast loss in single-particle electron cryomicroscopy. *Journal of Molecular Biology* **333**, 721–745 (2003).
63. Punjani, A., Rubinstein, J.L., Fleet, D.J. & Brubaker, M.A. cryoSPARC: algorithms for rapid unsupervised cryo-EM structure determination. *Nature Methods* **14**, 290+ (2017).
64. Sanchez-Garcia, R. et al. DeepEMhancer: a deep learning solution for cryo-EM volume post-processing. *Commun Biol* **4**, 874 (2021).
65. Kelley, L.A., Mezulis, S., Yates, C.M., Wass, M.N. & Sternberg, M.J.E. The Phyre2 web portal for protein modeling, prediction and analysis. *Nature Protocols* **10**, 845–858 (2015).
66. Roy, A., Kucukural, A. & Zhang, Y. I-TASSER: a unified platform for automated protein structure and function prediction. *Nature Protocols* **5**, 725–738 (2010).
67. Pettersen, E.F. et al. UCSF chimera - A visualization system for exploratory research and analysis. *Journal of Computational Chemistry* **25**, 1605–1612 (2004).
68. Lopez-Blanco, J.R. & Chacon, P. iMODFIT: Efficient and robust flexible fitting based on vibrational analysis in internal coordinates. *Journal of Structural Biology* **184**, 261–270 (2013).
69. Kidmose, R.T. et al. Namdinator - automatic molecular dynamics flexible fitting of structural models into cryo-EM and crystallography experimental maps. *Iucrj* **6**, 526–531 (2019).
70. Emsley, P., Lohkamp, B., Scott, W.G. & Cowtan, K. Features and development of Coot. *Acta Crystallographica Section D-Biological Crystallography* **66**, 486–501 (2010).
71. Jumper, J. et al. Highly accurate protein structure prediction with AlphaFold. *Nature* **596**, 583–589 (2021).
72. Tunyasuvunakool, K. et al. Highly accurate protein structure prediction for the human proteome. *Nature* **596**, 590–596 (2021).

## Methods

## Strains, plasmids and media

Yeast strains, plasmids, media and reagents are listed in Supplementary Table3.

## Yeast growth conditions

Yeasts were grown in complete synthetic media (CSM) buffered at pH 6.25 (Sorensen Buffer), lacking the appropriate(s) amino acid(s) to maintain plasmid(s) selection when necessary. Saturated yeast liquid pre-cultures grown in complete synthetic medium (CSM) were diluted into fresh CSM at OD<sub>600</sub> 0.3 and cultured 4 hours at 30°C to reach exponential growth (OD<sub>600</sub> 0.6) or 24 hours to reach Post Diauxic Shift (PDS). Confocal Z-stack images were acquired on LSM800 confocal microscope (Plan-Apochromat 63x/1.4 Oil Objective, Zeiss) at the relevant growth states.

For spot assays, exponentially growing cells were normalized to OD<sub>600</sub> 0.1, 5 µL from 4, serial 10-fold dilutions, were spotted on selective SC plates containing either rapamycin (at the indicated dilutions), Mohr salt (100 µM) or BPS (25 µM) and grown at 30 °C for 2-3 days. To measure the half-maximal effective concentration (EC<sub>50</sub>) of Rapamycin, plates were imaged and the intensity of each spot was measured using ImageJ. At each Rapamycin concentration, a relative growth coefficient was measured as the slope of the linear regression based on the intensities of the 4 dilution spots. The relative growth coefficients were then plotted as a function of the Rapamycin concentration and EC<sub>50</sub>s were extracted with Prism Software (version 8.3.0).

## Iron deprivation treatment

*EGO1*<sup>TEV</sup> cells transformed with a plasmid p(*CTH2p*)-3HA-TEV-(Cth2t) were grown overnight in buffered CSM-URA supplemented with 0.3 µM Mohr salt ((NH<sub>4</sub>)<sub>2</sub>Fe(SO<sub>4</sub>)<sub>2</sub>). Cultures were diluted to OD<sub>600</sub> 0.2-0.3 and grown for 5 hours before starting the iron deprivation treatment. This ensures the repression of the *CTH2* promoter. Cells was filtered with hydrophilic mixed cellulose esters membrane, 65 µm pore size and rinsed with buffered CSM-URA to wash out potential aggregates of Mohr salt. Cells were resuspended in buffered CSM-URA supplemented with 0.1 µM BPS and either imaged by confocal microscopy or harvested for immunoblotting assay at different time points during 90 minutes.

## Glucose deprivation and repletion

At OD<sub>600</sub> 0.6 cells growing exponentially at 30 °C in liquid CSM were filtered, washed once with starvation medium (CSM-glucose) and then transferred to CSM-glucose. 2% Glucose was subsequently added after 30 min of starvation. Confocal Z-stack images were acquired on LSM800 confocal microscope and/or aliquots for western blot analyses were taken at the relevant time points.

## Yeast Mating experiments

Experiments were performed by co-spotting equivalent amounts of exponentially growing *MATa* and *MATalpha* cells, onto a YPD plate and leaving it at 30°C for 2.5 hours. The yeast mixture was then

subsequently resuspended in liquid CSM at 30 °C and deposited on  $\mu$ -slides VI<sup>0.4</sup> channels (ibidi) coated with Concanavalin A (0.5mg/mL) to be subsequently imaged by Z-stacks or time-series (1 image/ 30 seconds) Z-stacks using TCS SP5 confocal microscope (Plan-Apochromat 63x/1.4 Oil Objective, Leica).

### **Light Microscopy and analyses**

All confocal images presented in the main and extended data are maximum projections of 3-5 images within a Z-stack (ImageJ). Z slices were initially separated by 500 nm. Image deconvolution was performed with Huygens Software. Analysis of TORC1 foci into size/volume classes followed 3D reconstructions of the stack image and intensity measurements using Imaris software<sup>27</sup>. The vacuolar enrichment of *EGO3-GFP*, *EGO1<sup>TEV</sup>* subjected to BPS treatment was measured with ImageJ. The mean intensity value in the cytosol was subtracted from the vacuolar membrane signal. The time of TOROID formation or dissolution upon EGOC depletion or replenishment was analysed with imageJ by measuring the intensity of TORC1 focus across the Z-stacks and over the duration of the acquisition. To quantify the degree of colocalization between TORC1 and EGOC, the intensity based colocalization function of Imaris Software was used to extract the Mander's and Pearson coefficients. Alternatively, measure of reciprocal puncta co-localisation was performed using cell segmentation (FIJI) followed by puncta segmentation according to their size in each channel (inferior or superior to 500 nm; Imaris). Signals from both channels were extracted and subjected to Pearson analysis to measure their correlation.

### **CrispR/Cas9 mutageneses**

pML104 plasmid expressing Cas9 enzyme and Guide RNA (from addgene) was linearized by PCR (Supplementary Table 3) and the 20-mer guide sequence targeting a specific yeast genome site was inserted by Gibson cloning<sup>54</sup>. Mutagenesis was achieved by genomic cut and recombination performed by co-transforming yeast strain with the specific plasmid and the codon optimized PCR product<sup>55</sup>. Short mutagenic PCR products (< 100 nucleotides) were obtained using overlapping forward and reverse primers (see Supplementary Table 2) while long mutagenic PCR products (> 100 nucleotides) were obtained using codon optimized gene sequences (GenScript; See Supplementary Table 3). Yeast were plated onto CSM-URA plates and then replicated on the same plates to decrease the number of false positive clones. CrispR efficiency was estimated by comparing the number of clones obtained with and without co-transformation with PCR product. 10 clones were then subjected to colony PCR (and subsequently sequenced to verify the mutagenesis. CrispR/Cas9 based Random PCR mutagenesis was performed using GeneMorphII Random Mutagenesis Kit (Agilent Technologies) aiming for 1-2 mutation(s) per 500 bp of PCR product. Transformants were plated onto 10-cm CSM-URA plates at a density of 100-200 clones per plate, and then replicated onto CSM-URA containing or not 2.5 nM Rapamycin. Rapamycin-sensitive clones were then sequenced using the same approach as previously described

### **Western Blot analysis**

Yeast cultures were treated following standard TCA-Urea extraction procedures. Protein lysates were loaded on a 4-20 gradient SDS-PAGE gel and transferred to a nitrocellulose membrane using the iBlot<sup>®</sup> system (ThermoFisher). The membrane was probed with primary antibodies overnight at 4 °C, washed and incubated with secondary antibodies for 45 min at RT. The membrane was developed using the Odyssey<sup>®</sup> imaging system (LI-COR) and the results were quantified using ImageStudio™ Lite (LI-COR).

Primary antibodies used were rabbit polyclonal anti-Sch9, mouse monoclonal anti-P-Sch9<sup>S758</sup> (*In house* at a dilution of 1:5'000 and 1:2'500, respectively) and mouse monoclonal anti-HA (1:15'000, Sigma n°H9658). Secondary antibodies used were donkey anti-rabbit, IRDye 800 (Li-Cor Biosciences) and donkey anti-mouse, IRDye 680 (Li-Cor Biosciences). All secondary antibodies were used at a dilution of 1:10'000.

### Plasmid design and protein purification

For the expression of all components of the EGO, two vectors were designed: one for the expression of EGO-TC and the second for the dimer of GTPases. Coding sequences of *EGO2(Δ 1-21)-EGO3-EGO1(Δ 1-111: His<sub>6</sub>)* were codon optimized for bacterial expression and synthesized by GenScript in pUC57. Each ORF was separated with an operon sequence (ttaactttaaaaaaaaaaaaaaacaggaggcaatatacat). The synthesized fragment was digested with NcoI and XhoI. The tricistronic ORF was cloned by T4 DNA ligation into a vector derived from pACYC (digested with NcoI and XhoI). The DNA sequences encoding full length *GTR1* and *GTR2* were amplified from *S. cerevisiae* gDNA (TB50 background). The bicistronic ORFs, separated by an operon sequence (aggaggaaaaaaa), was cloned by T4 DNA ligation into a pET-derived vector. Alternatively, plasmids carrying mutations that lock Gtr1 and Gtr2 in their active or inactive conformations (Q65L/S23L or S20L/Q66L, respectively) were used as template for the PCR<sup>25</sup>.

GTPases or all EGO components were (co)expressed in *E. coli* (BL21 DE3) and transformed cells were grown in 2xYT media at 37°C for 4 hours followed by overnight induction at 18°C with 0.1mM isopropyl-β-D-thiogalactopyranoside (IPTG). Cells were harvested by centrifugation and resuspended in lysis buffer for Ni-NTA purification [50mM Tris-Cl pH 7.4, 300mM NaCl, 5% Glycerol, 20mM Imidazole, 0.15% CHAPS, 1mM MgCl<sub>2</sub>, 1 μg/ml DNase, 1 μg/ml Lysozyme, supplemented with protease inhibitors 1mM PMSF and cOmplete™ Protease Inhibitor Cocktail] and lysed using an Emulsiflex system (AVESTIN). Total lysate was cleared by centrifugation at 15,000 rpm for 45 minutes at 4°C. The soluble fraction was subjected to an affinity purification using a chelating HiTrap FF crude column (GE Healthcare) charged with Ni<sup>2+</sup> ions on an AKTA-HPLC explorer. Proteins were washed and eluted in lysis buffer containing 250mM Imidazole. The purest fractions were concentrated to about 10mg/ml (Amicon 50kDA) and loaded on a Superdex GF200 Increase, equilibrated with the storage buffer [50mM MES-NaOH pH:6.0, 300mM NaCl, 0,15% CHAPS, 1mM MgCl<sub>2</sub>, 0,5mM DTT]. Purified proteins were concentrated to 1-1.8 mg/ml.

### Protein sequence Alignments

Protein sequence alignments were done using sequences from *Saccharomyces cerevisiae*, *Schizosaccharomyces pombe*, *Chaetomium thermophilum* and *Homo sapiens sapiens* and generated

with ClustalX2. Kog1 orthologue sequences: *S.c.* QHB09177, *S.p.* CAB08769, *C.t.* XP\_006691974 and *H.s.* Q8N122. Lst8 orthologue sequences: *S.c.* QHB11374, *S.p.* BAA32427, *C.t.* XP\_006696584 and *H.s.* Q9BVC4. TOR orthologue sequences: *S.c.* Tor1: CAA52849 and *S.c.* Tor2: CAA50548, *S.p.* Tor2: NP\_595359 and *S.p.* Tor1: NP\_596275, *C.t.* XP\_006695016 and *H.s.* mTOR P42345.

## 6x HIS Pull-down assay

Cells expressing *KOG1-TAP* or *kog1<sup>HC</sup>-TAP* were cultured in CSM and harvested either in exponential phase or PDS (OD<sub>600</sub> 2.5 or OD<sub>600</sub> 16, respectively). Cell pellets were frozen and further lysed by grinding in a cold mortar and pestle under liquid nitrogen. Cell extracts were resuspended in lysis buffer (50 mM Tris pH 7.4, 150 mM NaCl, 10 mM MgCl<sub>2</sub>, 0.1% NP-40, 1 mM PMSF, 3 tabs of cOmplete™ Protease Inhibitor Cocktail /100 mL of lysis buffer). Cell lysates were cleared by centrifugation at 4000 g at 4 °C for 10 min. Total protein concentrations were measured using Bradford protein assay and normalized to 5 mg/mL. Dynabeads® His-Tag Isolation & Pulldown (Novex) were washed once with binding buffer (50 mM Na-MES pH6, 600 mM NaCl, 1.5g/L CHAPS) and incubated with 20 µg of purified proteins (HIS<sub>6</sub>-GST or Ego2-Ego3-His<sub>6</sub>-Ego1, Gtr1&Gtr2) for 30 min at 4°C. Beads were washed once with lysis buffer and resuspended in the initial bead volume. For pull-down assays, 15 mg of total proteins and 25 µl microliters of coated Dynabeads were used per condition. The mixes were incubated for 60 min at 4 °C. The beads were washed 10 x with 2 ml ice-cold lysis buffer, boiled with 2 × SDS-PAGE sample buffer to elute the proteins and loaded onto 4–20% Mini-PROTEAN® TGX™ Precast Protein Gels. For immunoblot analysis, rabbit polyclonal anti-TAP (Open Biosystems CAB1001) and mouse monoclonal anti-polyHistidine antibody (clone HIS-1, Sigma H1029) were used at 1:2'000 and 1:4'000, respectively.

## CryoEM sample preparation

TORC1 filament samples were adsorbed for approximately 1 min onto Lacey carbon film grids (300 microMesh), blotted with Whatman filter paper according to the method described in <sup>56</sup>, and subsequently plunged in liquid ethane using a homemade plunging apparatus.

## CryoEM data collection

Cryo-EM images of TORC1 filaments were collected on a Titan Krios microscope (Thermo Scientific) at EMBL Heidelberg, Germany, operated at 300 kV and equipped with a K2 summit direct electron detector (Gatan) camera operated in counting mode. A total of 4901 movies of 16 frames were collected with a dose rate of 2.5 e-/Å<sup>2</sup>/s and a total exposure time of 8 s, corresponding to a total dose of 20 e-/Å<sup>2</sup>. Movies were collected at a magnification of 37,000x, corresponding to a calibrated pixel size of 1.35 Å/pixel at the specimen level.

## CryoEM data processing

Motion correction and dose weighting of the recorded movies were performed using MotionCor2 <sup>57</sup>, discarding the first frame. Initial CTF estimation was performed on the aligned and dose-weighted

summed frames using CTFFIND4<sup>58</sup>. TORC1 filaments were picked manually using the e2heliboxer module in EMAN2<sup>59</sup> from a total of 3864 micrographs, resulting in 8625 picked filaments. A total of 219,455 particles were extracted in RELION 2.0<sup>60</sup> using the `-helix` option, with an extract size of 600 pixels (810 Å), an outer diameter of 620 Å, and a helical rise of 26.75 Å. Following particle extraction, per-particle CTF correction was performed using Gctf<sup>61</sup>.

Initially, helical reconstruction was performed in RELION2.0 using binned particles (2.7 Å/pixel), a previously acquired low-resolution map of TOROID<sup>27</sup> low-pass filtered to 30 Å, and corresponding previously determined helical parameters as input, while imposing D1 symmetry and allowing for a helical symmetry search to optimize the respective helical parameters. The result of this helical reconstruction converged to a map with a resolution of around 9.1 Å based on the 0.143 gold-standard Fourier shell correlation (FSC) criterion<sup>62</sup>. 3D classification and subsequent helical refinement in RELION2.0 did not result in an increase in resolution. Next, we imported non-binned particles and the reconstructed map resampled to a voxel size of 1.35 Å in cryoSPARC 3.01<sup>63</sup>, and performed helical reconstruction imposing D1 symmetry, while allowing a helical symmetry search starting from the helical parameters obtained from the RELION helical reconstruction. The resulting 3D reconstruction had a resolution of 9.3 Å, similar to helical reconstruction in RELION. The broad peak of the mean squared error in a plot showing the estimated twist and rise (Figure S3A) indicates a relatively poor accuracy at determining the helical symmetry parameters on the un-symmetrized map of the last 3D refinement round. Indeed, similar scores are obtained for a twist ranging from approximately 46.9° to 47.7°, and rise from approximately 25.2 Å to 28.2 Å, which would translate into a pitch change from 201 to 205 Å and 192 to 215 Å, respectively (given an average twist for variable rise and vice versa).

We thus argued that the rather low resolution obtained after helical reconstruction in RELION and cryoSPARC could be the consequence of a varying pitch along the helices, resulting in an averaging of the structure while implying one set of helical parameters. To test this, we used the 9.1 Å helical reconstruction map (resampled to a voxel size of 1.35 Å) to create a mask containing the whole TOROID filament segment except for one central TORC1 assembly and its interacting regions with adjacent TORC1 complexes. We then performed signal subtraction in RELION2.0, using this mask and the structure and segment coordinates of the helical reconstruction, to generate a set of 219,455 subtracted particles containing one isolated TORC1 assembly per segment. Next, we employed the 'localrec' module in Scipion<sup>43,44</sup> to crop and re-center the signal subtracted particles in a smaller box of 300 pixels (405 Å), as well as assigning to each particle a refined defocus based on the helical geometry. Single-particle analysis (SPA) of the subtracted particles using 3D refinement in RELION2.0, while imposing D1 symmetry, resulted in a map with a resolution of 4.5 Å (FSC = 0.143). We then imported the particles from the RELION2.0 refinement in cryoSPARC 3.01. After 2D classification and class selection, a set of 213808 selected particles was used for Non-Uniform refinement<sup>45</sup> in cryoSPARC 3.01, employing a dynamic mask, imposing D1 symmetry, using the option to keep particles from the same helix in the same half-set, and allowing high-order aberration estimation and correction, which resulted in a final map with a resolution of 3.85 Å (FSC = 0.143). A final post-processed and locally sharpened map was obtained using

DeepEMhancer<sup>64</sup>. Local resolution estimation of the final 3D reconstruction was calculated in cryoSPARC 3.01. A summary of cryo-EM data collection parameters and image processing procedures can be found in Supplementary Information (Supplementary Figure 3, Supplementary Table 1).

## Model building and refinement

Initial homology models of Tor2 and Lst8 were generated using Phyre2<sup>65</sup>, while a model of Kog1 was generated using ITasser<sup>66</sup>. Homology models of Tor2, Lst8 and Kog1 were first manually placed in the final 3D reconstruction followed by rigid-body fitting in Chimera<sup>67</sup>. The rigid-body fitted models were subsequently subjected to a round of flexible fitting using Imodfit<sup>68</sup> followed by automatic molecular dynamics flexible fitting using NAMDINATOR<sup>69</sup>. The flexibly fitted structure was then refined using the Phenix software package (Adams et al., 2010) employing global minimization, local grid search, ADP refinement and secondary structure, Ramachandran and non-crystallographic symmetry (NCS) restraints. Initial refinement was followed by several cycles of extensive manual building in Coot<sup>70</sup> followed by additional rounds of refinement in Phenix using a nonbonded weight parameter of 200. A final refinement round was performed in Phenix using global minimization, local grid search, ADP refinement, secondary structure, Ramachandran and non-crystallographic symmetry (NCS) restraints, and a nonbonded weight parameter of 300.

AlphaFold<sup>71,72</sup> structural predictions for Kog1, Lst8, and Tor2 were released during preparation of this manuscript. Individual subunits within the built structural model of the TOROID assembly as well as the corresponding EM map density were thoroughly compared with the Kog1, Lst8 and Tor2 AlphaFold predictions. The AlphaFold structural prediction for Lst8 is virtually identical to Lst8 extracted from our TOROID structural model (RMSD: 0.882 Å over 259 aligned main-chain atoms). The AlphaFold Tor2 model is equally predicted well, but displays a closed conformation (similar to active mTOR, Figure 4B) starkly contrasting the open conformation of Tor2 extracted from our TOROID structural model, thus resulting in a RMSD value of 8.484 Å (1894 aligned main-chain atoms). While the Kog1 AlphaFold model shows a high overall agreement with Kog1 extracted from the TOROID structure (RMSD: 0.829 Å over 1016 aligned main-chain atoms), the 'Twix' region displays a tilt which markedly differs from the TOROID structure, and the 'Tack' region, although correctly predicted as a helix surrounded by large loop regions, is predicted to be in a completely incorrect location. Accordingly, the model confidence score of this particular region in the Kog1 AlphaFold structural prediction is very low. Nonetheless, we were able to use the Kog1 AlphaFold model to improve the TOROID Kog1 structure in regions where the EM density was very weak, notably the Kog1 N-terminus and the C-terminal WD domain, resulting in significantly improved protein geometry validation statistics. A summary of refinement and validation statistics can be found in Supplementary Table 1.

## Data Availability

Cryo-EM TOROID maps obtained using either helical reconstruction or signal subtraction and ensuing single particle analysis have been submitted to the EM Data Bank (EMDB) with accession codes EMD

13595 and 13594 respectively. The atomic model built in the signal subtracted TOROID cryo-EM map is submitted to the Protein Data Bank (PDB) with accession code 7PQH.

## Figures

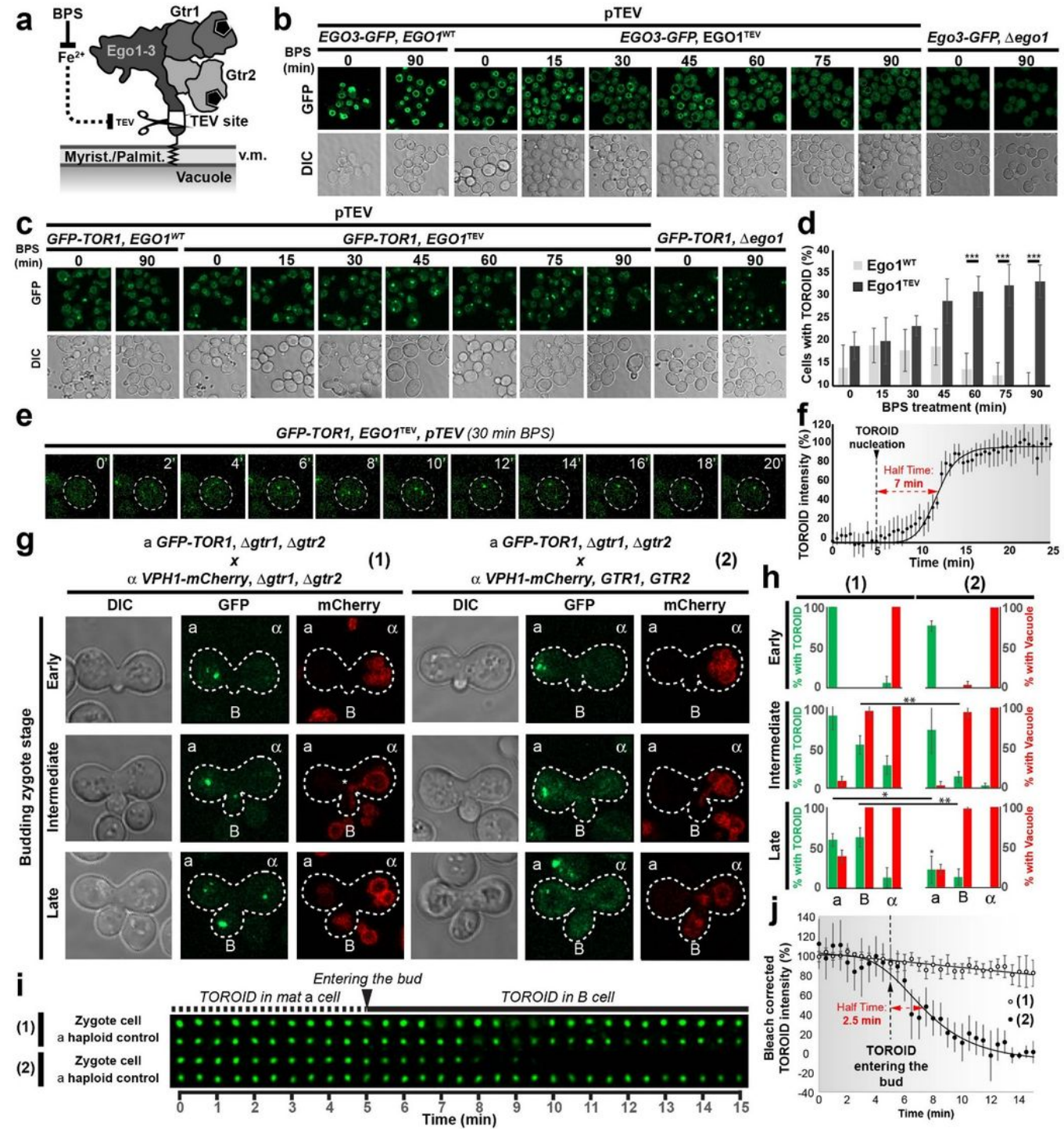


**FIGURE 1**

Figure 1

**Acute removal / restoration of the EGOC from the vacuole membrane contemporaneously induces TOROID formation / dissolution. a)** Schematic describing the strategy to shave EGOC off of the vacuole membrane. **b)** EGOC (Ego3-GFP) localisation in Ego1<sup>WT</sup> and Ego1<sup>TEV</sup> strains following TEV protease induction and in *Dego1* strain as control lacking vacuolar localisation. **c)** TORC1 (GFP-TOR1) monitored in the strains described in b. **d)** Quantification of data represented in c. (N=3, n>600 cells). **d,f,h,j)** Error bars represent the standard deviation. P-values are represented by symbols as: \*\*\*<0.001, \*\*<0.01 and \* <0.05. **e)** Single cell analyses after 30 min of TEV induction in a *GFP-TOR1, ego1<sup>TEV</sup>*. Time lapses in minutes. **f)** Quantification of data represented in e (N= 30 individual TOROIDS). **g)** TOROID dynamics upon EGOC restoration in three mating stages: Early, Intermediate, and Late. *MATa GFP-TOR1* strain (**a**) is crossed with *MATalpha* mating *VPH1-mCherry* strain (**a**) which carries either (1) *Dgtr1 gtr2* or (2) *GTR1 GTR2*. (**B**) indicates the bud of the zygote. **h)** Percentage of **a, a** and **B cells** containing a TOROID and Vph1-mCherry-marked vacuoles from data presented in g (N= 30 matings). **i)** Kymographs tracking TOROID dynamics upon matings in g. **a** cells not engaged in a mating are used as bleaching controls. **j)** Quantification of data represented in i (N= 30 individual matings).

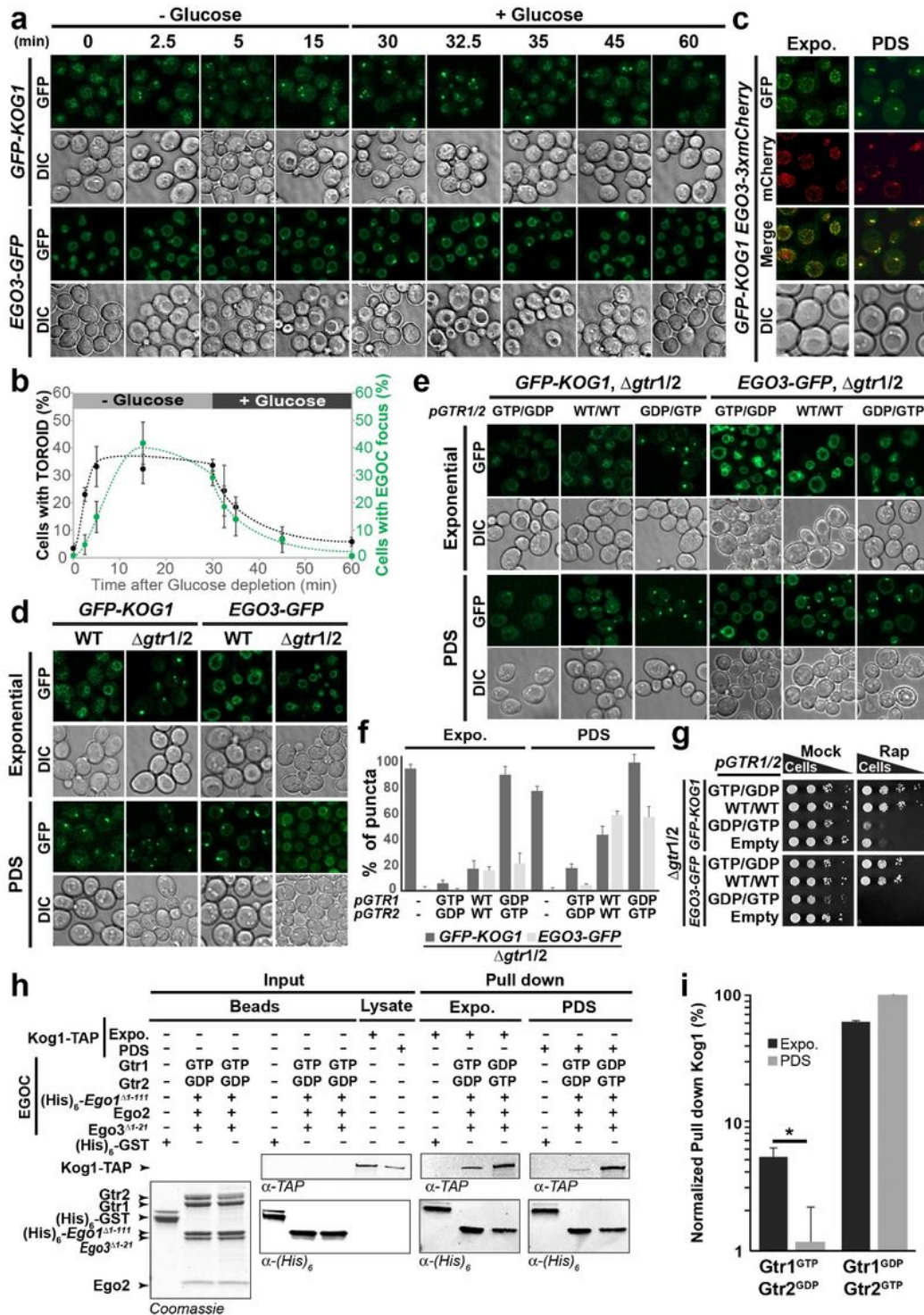


**FIGURE 2**

Figure 2

**EGOC and TORC1 form co-localized and inter-dependent puncta.** **a)** GFP-Kog1 or Ego3-GFP cells following glucose depletion and subsequent re-addition. **b)** Plot representing the quantification of puncta formation from **a)**. (N=3; n>500 cells for GFP-Kog1 and n>200 cells for Ego3-GFP). **b,f,i)** Error bars represent the standard deviations. P-values are represented by symbols as: \*<0.05. **c)** GFP-Kog1 and Ego3-3xmCherry cells. **c,d,e)** cells were imaged in exponential phase or PDS. **d)** GFP-Kog1 or Ego3-GFP, in

WT or in  $\Delta gtr1 \Delta gtr2$  cells. **e)** GFP-Kog1 or Ego3-GFP  $\Delta gtr1 \Delta gtr2$  cells were co-transformed with  $pGTR1^{WT}/pGTR2^{WT}$ ,  $pGTR1^{GTP}/pGTR2^{GDP}$  or  $pGTR1^{GDP}/pGTR2^{GTP}$  plasmids. **f)** Bar graph representing the quantification of puncta formation (TOROID and EGOC) from e). (N=3, n> 500 cells). **g)** Cells with the indicated genotypes spotted onto plates containing 2.5 nM Rapamycin. **h)** *In vitro* pull down of TORC1, purified from exponential or PDS cultures, using recombinant EGOC containing either “active” (Gtr1<sup>GTP</sup>/Gtr2<sup>GDP</sup>) or “inactive” (Gtr1<sup>GDP</sup>/Gtr2<sup>GTP</sup>) GTPase dimer. (His)<sub>6</sub> purified proteins are shown in Coomassie-stained SDS PAGE-Gel. Input and pull down are shown by western blotting using primary antibodies to detect the corresponding proteins. **i)** Quantification of the relative TORC1 pull down efficiency from h). (N=3).

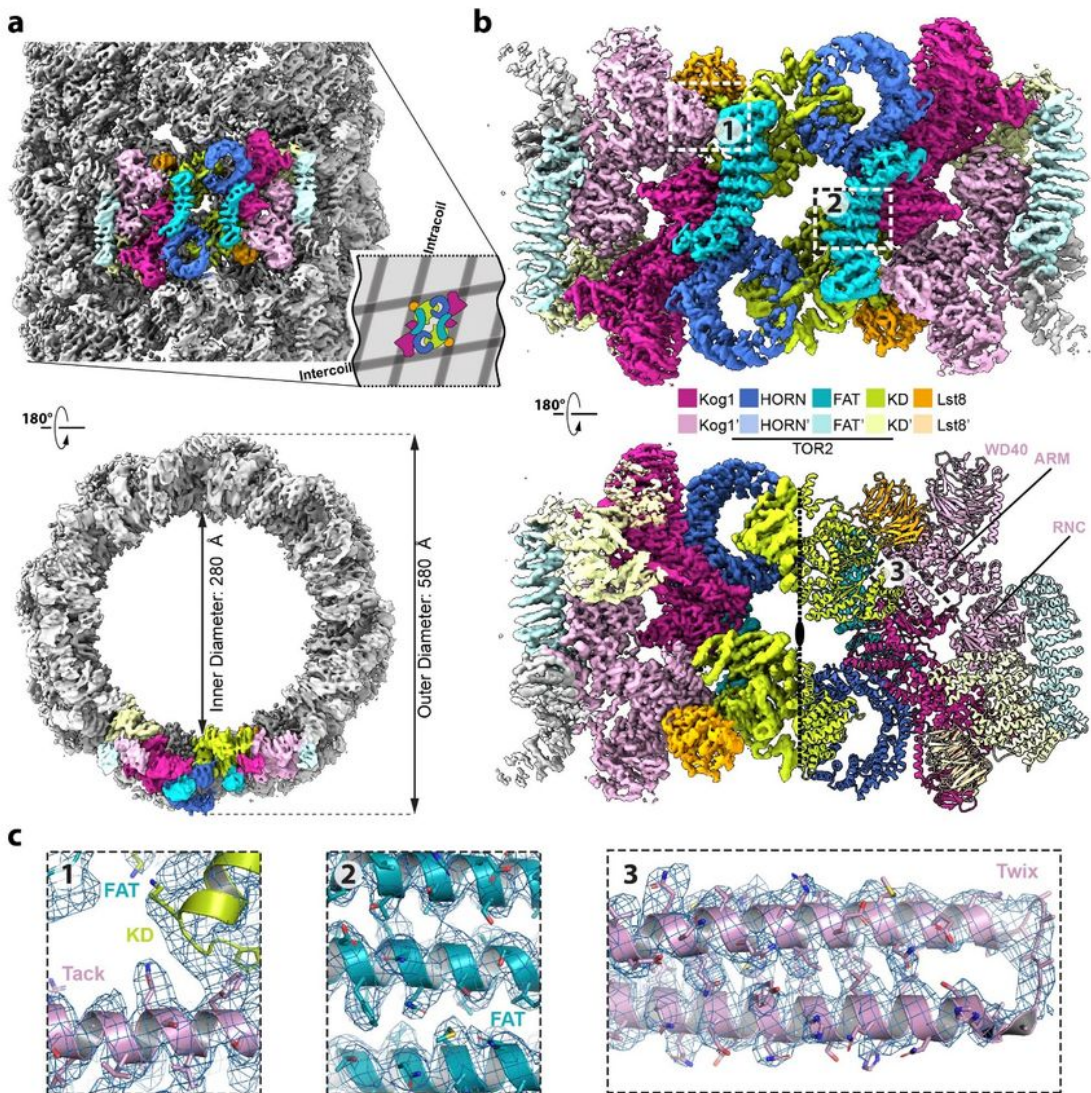


**FIGURE 3**

**Figure 3**

**TOROID Cryo-EM reconstruction. a)** Helical reconstruction TOROID map. **b)** Cryo-EM reconstruction of TOROID via signal subtraction and single particle analysis (SPA). **a-c)** Colouring corresponds to different TORC1 subunits as indicated in b). **c)** Zoomed views from b) showing a cartoon representation of the atomic TORC1 model, built in the Cryo-EM map (blue mesh). Selected amino acid residues are represented as sticks.

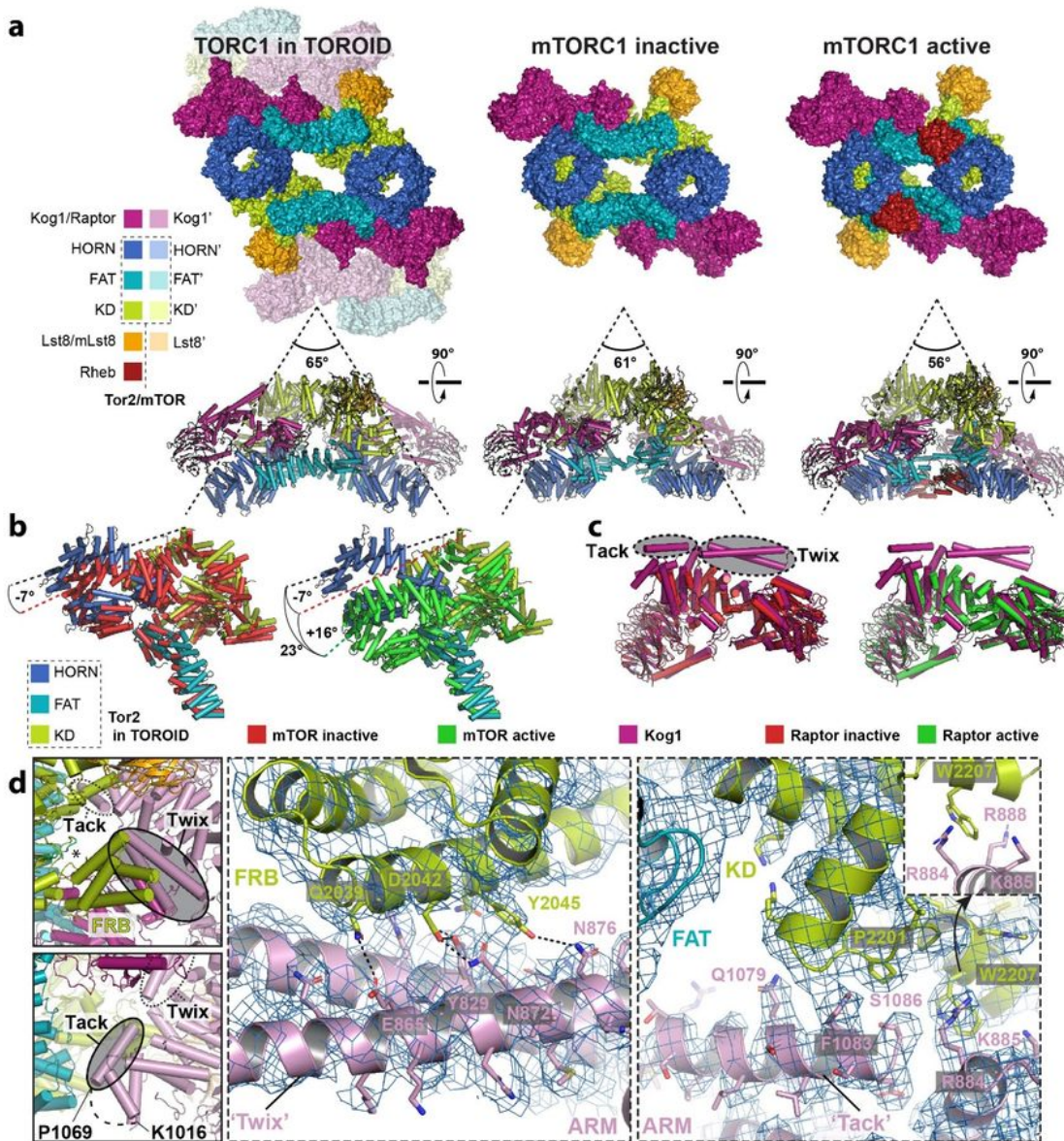


**FIGURE 4**

**Figure 4**

**TORC1 adopts an inactive conformation in TOROIDs.** **a)** Views of TORC1 in a TOROID (left), inactive mTORC1 (middle, PDB ID: 6BCX) and active mTORC1 bound to Rheb (right, PDB ID: 6BCU). **a-d)** Colouring of TORC1 subunits is performed according to the scheme in **a**. **b)** Structural alignment of Tor2 in TOROID with mTOR from inactive mTORC1 and mTOR from active mTORC1/Rheb. **c)** Structural alignment of Kog1 in TOROID with Raptor from inactive mTORC1 and Raptor from active mTORC1/Rheb. **d)** Insets

showing a zoom of the hub of interactions between Kog1 and Tor2'. Zoomed views from b) showing a cartoon representation of the atomic TORC1 model, built in the Cryo-EM map (blue mesh). Selected amino acid residues are represented as sticks.

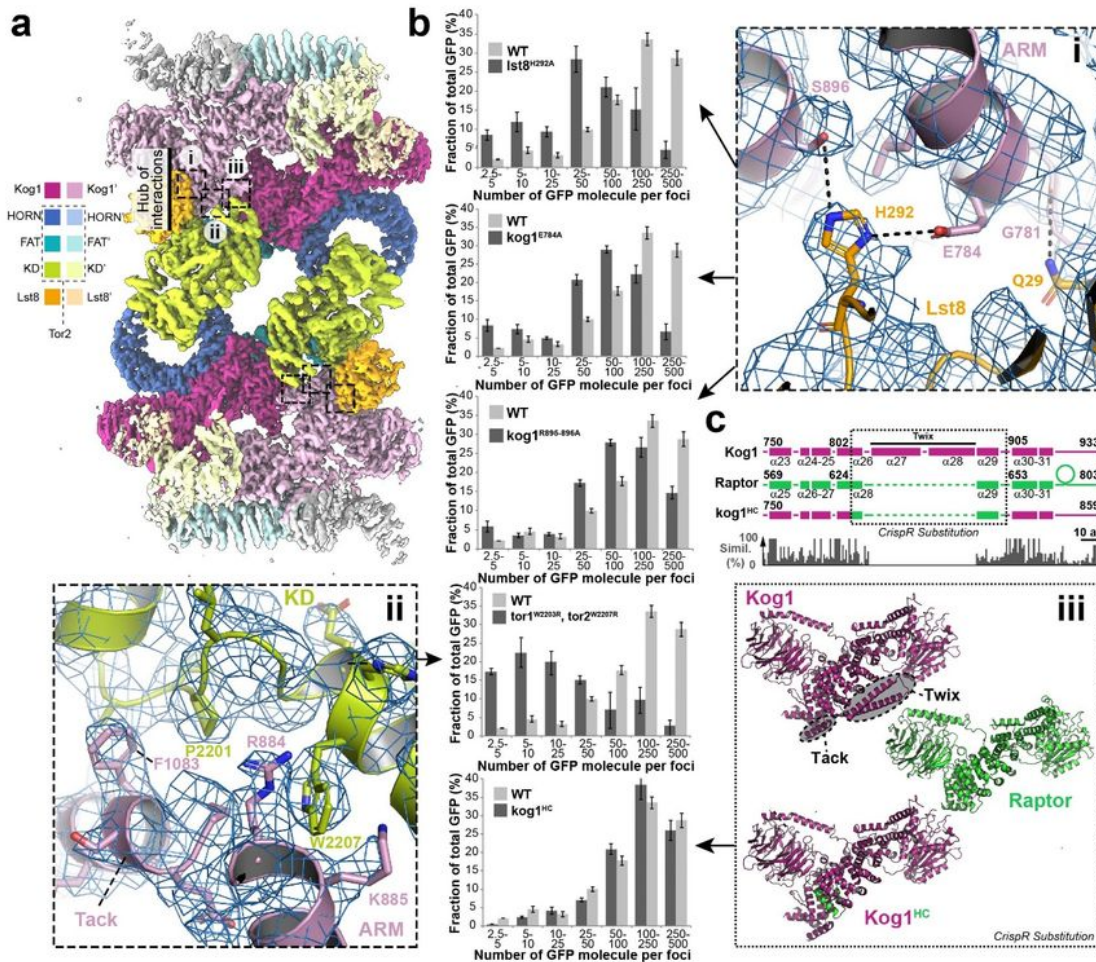


**FIGURE 5**

Figure 5

**Crispr/Cas9 mutations to test intra- and inter-coil TORC1-TORC1' interactions. a)** TORC1 molecular model extracted from the TOROID Cryo-EM map. Adjacent protomers are shown in light and dark colours. Dashed boxes (i, ii, iii) indicate the regions mutagenized to validate the TORC1-TORC1' hub of interactions. **b-c)** TORC1 focus size distributions measured in PDS cells harbouring the indicated mutations. The control data are the same in all panels. **c)** Alignment of Kog1, Raptor and Kog1<sup>HC</sup>. Alpha helices are numbered according to the molecular model.

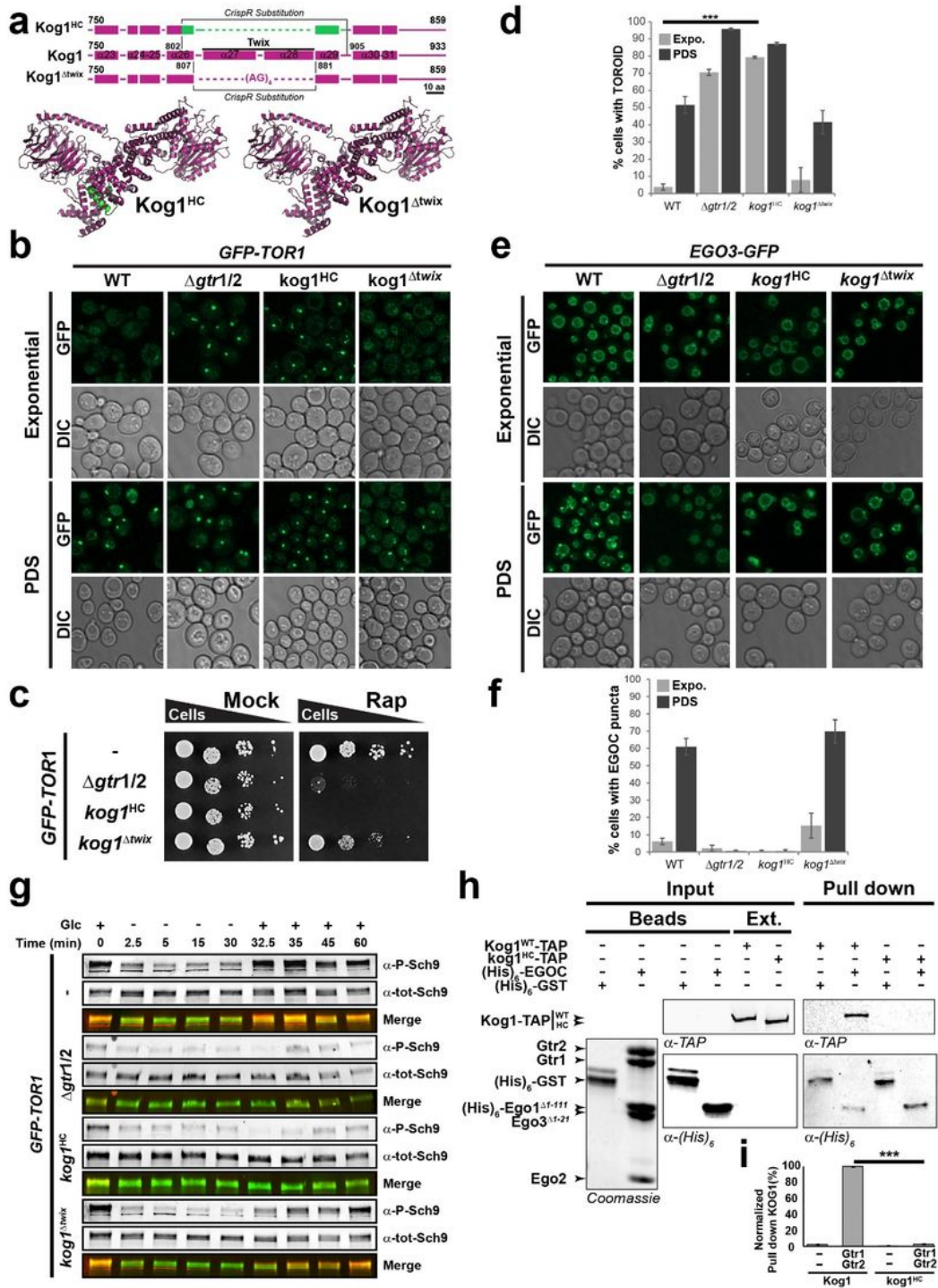


**FIGURE 6**

## Figure 6

**Helices a26 and a29 of Kog1 are required for interaction with the EGOC.** **a)** Alignment of Kog1, Kog1 <sup>$\Delta$ twix</sup> and Kog1<sup>HC</sup> sequences and corresponding structure models. Alpha helices are numbered according to the molecular model. **b,e)** *WT*,  *$\Delta$ gtr1  $\Delta$ gtr2*, *kog1<sup>HC</sup>* and *kog1 <sup>$\Delta$ twix</sup>* cells expressing GFP-Tor1 b) or Ego3-GFP e) in exponential phase or in PDS. **c)** Cells with the indicated genotypes spotted onto plates containing 2.5 nM Rapamycin. **d,f)** Bar graph representing the quantification of TOROID or EGOC puncta formation from b) and e) respectively (N=3 and n>300). Error bars correspond to standard deviation and \*\*\*<0.001. **g)** Western blot analysis of glucose-dependent TORC1 activity using the indicated strains. **h)** *In vitro* pull downs of TORC1 containing either Kog1-TAP or Kog1<sup>HC</sup>-TAP using cobalt-Dynabeads pre-coated with purified (His)<sub>6</sub>-proteins (Coomassie). Inputs and Pull Downs were analyzed by western blot. **i)** Quantification of h) with N=3. Error bars correspond to standard deviation. \*\*\* indicates P-value lower than 0.001.

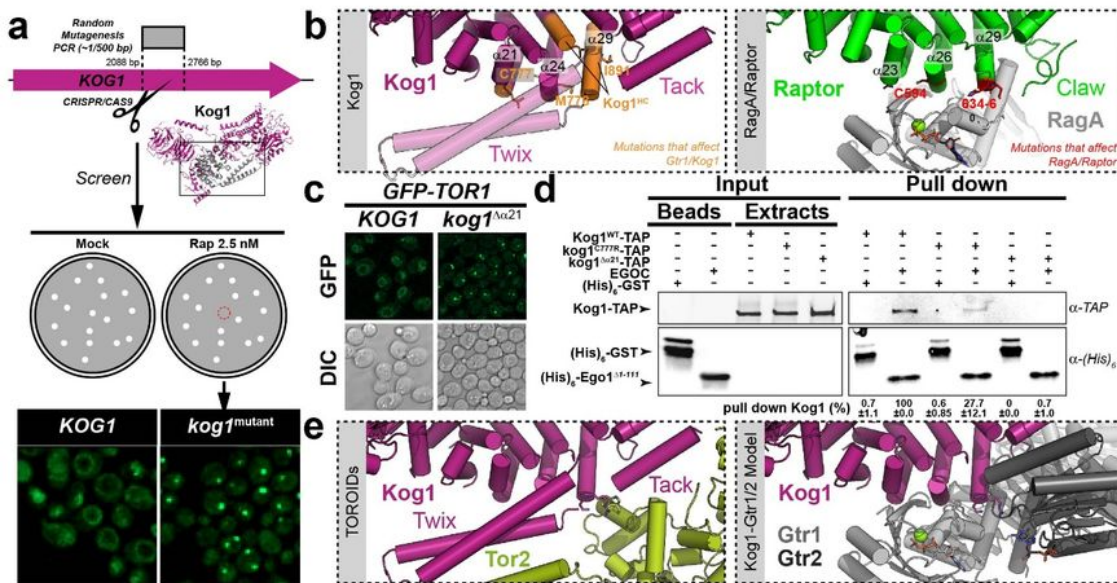


**FIGURE 7**

**Figure 7**

Random mutagenesis reveals that EGO binding to Kog1 competes with TORC1 oligomerisation. **a)** Schematic representing the random mutagenesis screen of the *KOG1<sup>armadillo</sup>* sequence to uncover constitutive TOROID mutants. **b)** Left panel: Location of mutations in Kog1. Right panel: Location amino acids in Raptor that when altered disrupt RagA binding (Rogala et al., 2019). **c)** Effect of Kog1 helix a21 deletion (*kog1<sup>Da21</sup>*) on TORC1 (GFP-Tor1) localisation in exponential phase. **d)** *In vitro* pull downs of

TORC1 containing either Kog1<sup>WT</sup>-TAP or Kog1<sup>C777R</sup>-TAP or Kog1<sup>Da21</sup>-TAP using cobalt-Dynabeads pre-coated with purified (His)<sub>6</sub>-proteins (Coomassie). Inputs and Pull Downs were analyzed by western blot using corresponding antibodies. **e)** EGOC and Tor1/2 compete for the same region within Kog1. Left panel: View of Kog1 interacting with Tor2' as determined from our TOROID structure. Right panel: View of Kog1 interacting with Gtr1 and Gtr2 modelled from the Raptor-RagA/C structure and supported by our extensive mutagenesis experiments.

## Supplementary Files

This is a list of supplementary files associated with this preprint. Click to download.

- [SupplementaryTable1.docx](#)
- [SupplementaryTable2.docx](#)
- [SupplementaryTable3.docx](#)
- [floatimage8.jpeg](#)
- [floatimage9.jpeg](#)
- [floatimage10.jpeg](#)
- [floatimage11.jpeg](#)
- [floatimage12.jpeg](#)
- [floatimage13.jpeg](#)
- [FigureS7.pdf](#)